Geochemistry, Geophysics, Geosystems®

AGU ADVANCING EARTH AND SPACE SCIENCE

RESEARCH ARTICLE
10.1029/2021GC009930

Key Points:

- First estimates of paleosecular variation (PSV) across the entire Triassic period using a new paleomagnetic database
- PSV and its latitudinal dependence barely changed throughout the time interval between the two most recent superchrons (264-126 Ma)
- Distinctive PSV behavior indicates that the Permo-Carboniferous Reversed Superchron field had enhanced axial dipole dominance

Supporting Information:

Supporting Information may be found in the online version of this article.

Correspondence to:

B. T. Handford,
b.handford@liverpool.ac.uk

Citation:

Handford, B. T., Biggin, A. J., Haldan, M. M., & Langereis, C. G. (2021). Analyzing Triassic and Permian geomagnetic paleosecular variation and the implications for ancient field morphology. *Geochemistry, Geophysics, Geosystems*, *22*, e2021GC009930. https://doi.org/10.1029/2021GC009930

Received 2 JUN 2021
Accepted 4 NOV 2021

Author Contributions:

Conceptualization: B. T. Handford, A. J. Biggin, C. G. Langereis
Data curation: B. T. Handford, M. M. Haldan
Funding acquisition: A. J. Biggin, C. G. Langereis
Investigation: B. T. Handford, M. M. Haldan
Methodology: B. T. Handford
Resources: B. T. Handford
Software: B. T. Handford, A. J. Biggin
Supervision: A. J. Biggin, C. G. Langereis

Analyzing Triassic and Permian Geomagnetic Paleosecular Variation and the Implications for Ancient Field Morphology

B. T. Handford[1], A. J. Biggin[1], M. M. Haldan[2], and C. G. Langereis[2]

[1]Department of Earth, Ocean and Ecological Sciences, University of Liverpool, Liverpool, UK, [2]Paleomagnetic Laboratory Fort Hoofddijk, Utrecht University, Utrecht, The Netherlands

Abstract Studying paleosecular variation (PSV) can provide unique insights into the average morphology of the geomagnetic field and the operation of the geodynamo. Although recent studies have expanded our knowledge of paleomagnetic field behavior through the late Mesozoic, relatively little is known regarding the Triassic period (ca. 251.9–201.3 Ma). This study compiles the first Triassic virtual geomagnetic pole (VGP) database for the analysis of PSV, as part of a longer Post-Permo-Carboniferous Reversed Superchron (PCRS) time interval (265-198 Ma). VGP angular dispersion and its dependence on apparent paleolatitude are compared against a new PCRS compilation and published PSV compilations for intervals across the last ~320 Ma. We find that the Post-PCRS displays near latitudinal invariance of VGP dispersion while the PCRS displays very strong latitudinal dependence. PSV behavior during the Post-PCRS appears indistinguishable to that previously reported for the interval preceding the Cretaceous Normal Superchron (Pre-CNS; 126–198 Ma). The near-constant behavior between time intervals with significantly different apparent average polarity reversal frequencies does not support a suggested relationship between VGP dispersion and reversal frequency. The dispersion observed for the PCRS is consistent with the results of previous studies and represents behavior that is potentially unique over the last ~320 Ma. A recently published approach to obtain a description of field morphology from equatorial VGP dispersion shows the PCRS geomagnetic field to have been more strongly axial dipole dominated than any interval since. This observation may be causally linked to the PCRS being the longest known superchron in the Phanerozoic geomagnetic polarity timescale.

Plain Language Summary Understanding how the stability of the Earth's magnetic field has changed throughout Earth's history provides insight into the evolution of the internal, dynamic processes that generate the geomagnetic field. This study is the first to analyze such behavior during the Triassic, occurring approximately 251.9–201.3 million years ago, and compares this behavior against that during other intervals over the last 320 million years. These intervals represent times when the magnetic field was reversing polarity at different rates. This study found similar behavior between two adjacent time intervals that each display very different reversal rates, suggesting any possible relationship to be more complex than previously thought. We also show that, during the longest known interval over the last 320 million years without reversals, the field more closely resembled that of a bar magnet aligned with the Earth's rotation axis. This result offers a possible explanation as to why it is longer than similar intervals without reversals.

1. Introduction

The geomagnetic field exists as a consequence of a dynamic system and shows variations across a range of timescales (Johnson & McFadden, 2015). Long-term behavior is often described in terms of the intensity, reversal rate, morphology, and stability of the field. As all of these features are a result of the geodynamo, it follows that their variations should be intrinsically linked and that relationships may exist between them (Biggin et al., 2008; Gubbins, 1987; McFadden et al., 1991; Pal, 1991; Sprain et al., 2016; Tarduno et al., 2001). Identifying such relationships could allow for inferences regarding one aspect of the Earth's field behavior, for which there is a sparse data population, based on knowledge of another over the same time. This could be of particular use in characterizing reversal frequency and in providing a constraint on core-mantle interactions (Biggin et al., 2012). Obtaining a direct understanding of reversal frequency

Writing – original draft: B. T. Handford
Writing – review & editing: A. J. Biggin

requires complete and ideally well-dated magnetostratigraphic sections which are not available for most of Earth's history (Ogg, 2012). This is particularly the case for the Precambrian as biostratigraphy cannot be used and radiometric dating comes with large uncertainties (Bleeker, 2004). There is also the potential to obtain a greater understanding of geodynamo evolution. Periodic variations in the reversal record have been observed on similar time-scales to those of mantle processes; this constitutes support for the hypothesis that core-mantle boundary (CMB) heat flux variations influence geomagnetic field behavior (Biggin et al., 2012; Tarduno & Cottrell, 2005).

Earth's polarity reversal record is largely well-defined since the latest Carboniferous (~320 Ma; Hounslow et al., 2018) and demonstrates extreme long-term variations. During superchrons, reversals are essentially absent and the Earth's magnetic field exhibits a stable polarity for tens of millions of years. Two such events have been identified in the last 350 Ma, the Permo-Carboniferous Reversed Superchron (PCRS; ~318-265 Ma; Haldan et al., 2009; Opdyke & Channell, 1996), and the Cretaceous Normal Superchron (CNS; 126-84 Ma; Ogg, 2012). In contrast, an apparent average reversal rate of ~11 per Myr (Myr^{-1}; Ogg, 2012) is assigned to a time interval referred to as the Jurassic hyperactivity period (~171-155 Ma; Ogg, 2012). The Triassic (ca. 251.9–201.3 Ma; Ogg, 2012) has a relatively incomplete reversal record (Hounslow et al., 2018). Although it is sufficiently well understood to provide accurate estimates of reversal frequency across the entire period, its incomplete nature has resulted in various proposed magnetostratigraphic sequences (Hounslow & Muttoni, 2010; Hounslow et al., 2018; Maron et al., 2019). The lack of an agreed upon geomagnetic polarity timescale (GPTS) for the Triassic has hindered its use for timescale definition, spawning the suggestion to describe Triassic magnetostratigraphy as a set of multichrons (Lucas, 2010; Lucas & Tanner, 2014). Such a description would contain less information than would be available from traditional chron to chron correlation, highlighting that although the number of reversals occurring during the Triassic is reasonably well constrained, the exact ages of the reversals are not.

The Earth's magnetic field is often described as a geocentric axial dipole (GAD). This description is believed to be accurate when a sufficient amount of time can be averaged (Schneider & Kent, 1990) but non-dipole contributions are ever present in the instantaneous field configuration. Studying the dispersion of virtual geomagnetic poles (VGPs) can provide an estimate of the extent of this contribution (Biggin et al., 2020; Veikkolainen & Pesonen, 2014). Analyzing PSV in this way provides a measure of field stability and many recent studies have investigated a possible association between PSV and reversal frequency (Biggin et al., 2008; de Oliveira et al., 2018; Doubrovine et al., 2019; Franco et al., 2019; Veikkolainen & Pesonen, 2014).

Investigations into the relationship between PSV and reversal frequency have tended to focus on the CNS, PCRS, and Jurassic due to their nature as extreme high and low reversal frequency regimes (Biggin et al., 2008; de Oliveira et al., 2018; Doubrovine et al., 2019). Similarly, Franco et al. (2019) investigated PSV in the Illawarra Hyperzone of Mixed Polarity (IHMP; ~266.7–228.7 Ma), beginning after the PCRS, stating an average reversal rate of ~5.9 Myr^{-1}. Many of these studies have focused on sequential time periods resulting in a near continuous record of VGP dispersion from the CNS going back to the PCRS, with the exception of almost the entirety of the Triassic. Despite this, it is still unclear whether a relationship does exist between PSV and reversal frequency. McFadden et al. (1991) concluded that low reversal regimes would exhibit lower VGP dispersion at low latitudes, and a high latitudinal dependence. Both Biggin et al. (2008) and Doubrovine et al. (2019) described the occurrence of this behavior during the CNS, while de Oliveira et al. (2018) obtained a similar, more extreme result for the PCRS. Other results suggest near latitudinal invariance during the Jurassic (Doubrovine et al., 2019) and IHMP (Franco et al., 2019) and therefore, it might be claimed that studies of extreme reversal regimes support the original claim of McFadden et al. (1991). Discrepancies appear when comparing these results with those from more recent time intervals, however Doubrovine et al. (2019) found that the relationship between PSV and latitude for the last 5 or 10 Ma was similar to that observed for the superchrons, despite average reversal frequencies of ~4.4–4.8 Myr^{-1}. In contrast, Franco et al. (2019) concluded that the last 5 Ma exhibited comparable behavior, and a similar reversal rate, to that which they described for the IHMP.

In addition to our lack of knowledge regarding PSV behavior during the Triassic, and historically uncertain magnetostratigraphy, there is a significant shortage of paleointensity data for this period. The Triassic is a period bounded by mass extinction events that coincided with eruptions of huge volumes of flood basalts (Ogg et al., 2016). It also comprises an interval of time in which all continents were arranged as

the supercontinent Pangaea, with peak assembly during the middle Triassic (Lucas, 2005). This tectonic setting resulted in little large-scale volcanism after the Siberian Traps (ca. 252-251 Ma; Burgess et al., 2017; Wignall, 2015) until the eruption of the Central Atlantic Magmatic Province (CAMP; ca. 201.5 Ma; Ogg et al., 2016), associated with the break-up of Pangaea (Benton, 2016). This provides an explanation as to why a relatively minor proportion of known Triassic rocks are volcanic (Lucas, 2005). As a result, there is a ~50 Ma gap in the paleointensity record (Anwar et al., 2016) due to the nature of absolute paleointensity experiments which are heavily reliant on volcanic recorders and their associated intrusions (Donadini et al., 2007; Lerner et al., 2017). An incomplete reversal record, very few paleointensity estimates, and a lack of PSV analysis have all resulted in a limited understanding of geomagnetic field behavior during the Triassic when compared to other periods since the latest Carboniferous. As we will demonstrate here, however, there are a sufficient number of Triassic-aged rapidly cooled igneous units distributed globally to provide a first order description of the geomagnetic field through this period.

The last decade has provided many investigations into Triassic magnetostratigraphy with sufficient progress to justify a revised Triassic GPTS (Haque et al., 2021; Kent et al., 2017, 2018, 2019; M. Li et al., 2016; Maron et al., 2019; Zhang et al., 2020). These advancements present the opportunity to analyze Triassic PSV behavior within the context of the average reversal frequency for the period. Such an investigation would result in a continuous record describing PSV behavior from the PCRS through to the CNS, whilst also facilitating an investigation into PSV behavior between two prominent features of the reversal record: the PCRS and the high reversal rate values associated with the Jurassic. At the same time this offers the potential to categorize geomagnetic field behavior during a time period still characterized by much uncertainty. In this study, an updated Triassic paleomagnetic directional and VGP database is presented, using results taken from existing publications, and combined with data previously compiled for the late Permian. An analysis of VGP dispersion at different paleolatitudes for this newly studied time interval, (265 - 198 Ma) referred to as the "Post-PCRS," is compared to data from a revised PCRS database using the same analytical process. Furthermore, comparisons are then carried out against previously published databases for the Pre-CNS (198 - 126 Ma), CNS (Doubrovine et al., 2019), and the last 10 Ma (Cromwell et al., 2018) before a discussion on the pattern of VGP dispersion with latitude during times of differing reversal frequencies and how this may relate to field morphology.

2. Method

2.1. Sourcing Data

Information from PSV analysis comes in two distinct forms: time series of magnetic field variations, such as information from long sediment cores, and statistical descriptions which rely on geologically instantaneous spot readings, such as those associated with lava flows (Johnson & McFadden, 2015). Data derived from sedimentary rocks are susceptible to smoothing of the recorded field during remanence acquisition, resulting in at least partial averaging of PSV (Lund & Keigwin, 1994) and inclination shallowing, affecting the final estimate of paleolatitude (Tauxe & Kent, 2004). The general consensus is that igneous rocks, and in particular volcanic rocks, are a more reliable source of PSV information in older geologic periods (Biggin et al., 2008; Cromwell et al., 2018; McFadden et al., 1988), provided that they cooled quickly and that the group of rocks spans sufficient time to provide representative variability. As such this study exclusively uses data from igneous rocks, avoiding large, slow cooling intrusions that would not provide a spot-reading of the field. All datasets have been taken from lava flows, sills, dykes, or pyroclastic flow deposits with supporting evidence for fast cooling rates where appropriate and for the occurrence of welding when pyroclastic flow deposits have been used.

Triassic datasets were compiled from papers published up to and including those from March 2020. Most data arose from a literary search but a small number of datasets were sourced using the Global Paleomagnetic Database (iggl.no/resources.html, Ivar Giæver Geomagnetic Laboratory). Datasets from the late Permian, after the PCRS, were sourced from the database compiled by Franco et al. (2019). The revised PCRS database was built around the work of de Oliveira et al. (2018) with the addition of a few new datasets. Following the approach of Biggin et al. (2008) site-mean directions of a similar age and geographic location were grouped into the same data set.

After these initial constraints, both the PCRS and Post-PCRS databases were filtered using selection criteria in order to remove low quality data and potentially unsuitable studies. This study applied the selection criteria below. These are the same as used by Doubrovine et al. (2019) but with a few additional requirements.

1. The age of the rock formation must be reasonably well constrained, preferably by the application of radiometric dating techniques. There must be no doubts that the data set might not represent the geomagnetic field during the time interval to which it has been assigned that is the PCRS or Post-PCRS.
2. There must be no evidence that the characteristic remanent magnetisation (ChRM) directions are of secondary origin.
3. Data from igneous formations that were tectonically tilted or folded post-emplacement must have an associated structural correction. Where there was evidence of local block rotation between sampling sites, data were not used. A commentary outlining the reasoning behind the inclusion of each data set, with respect to its tectonic setting, can be found in Table S2.
4. Each data set is composed of at least nine paleomagnetic sites ($N \geq 9$), and each site-mean direction is calculated from the ChRM of a minimum of 3 independently oriented samples ($n \geq 3$).
5. ChRM components must have been isolated using stepwise demagnetization techniques. Principal component analysis should have been utilized for at least one specimen per site and agree with any ChRM components inferred by other methods. This corresponds to a "demagnetization code" greater than or equal to 3 (McElhinny & McFadden, 2000).
6. The uncertainties of the site-mean directions must be presented in the original study as either the Fisher concentration parameter (k) or the angle of 95% confidence about the mean direction (α_{95}).
7. The total Q score based on the first 6 Van der Voo criteria must be equal to or greater than 3.
8. All site-mean ChRM directions within a data set have a k-value greater than or equal to 10.

In Supporting Information S1, the effects of accounting for serial correlation and the removal of data derived from great circle analysis were considered, separately, for datasets which satisfied selection criteria 1–8. Serial correlation identifies cooling units that are likely representative of the same event in time, and as such may not be considered as individual paleomagnetic data points (Cromwell et al., 2018; Watson & Beran, 1967). Meanwhile, obtaining directions from great circle analysis often results in the inability to obtain rigorous confidence limits for K (McFadden & McElhinny, 1988). The inclusion of great circle derived data has the potential to allow datasets to fulfill selection criteria 1–8 which may not have a well-defined Fisher concentration parameter and thus could be of lower quality than desired. In both cases the overall effects on the calculated VGP dispersions were minor (Figures S1 and S2 in Supporting Information S1). As a result, neither the inclusion of serial correlation or the exclusion of great circle derived data was utilized in the final data selection process due to the benefits associated with a greater N, and total number of datasets (Biggin et al., 2008).

2.2. Investigating Robustness With Additional Criteria

McElhinny and McFadden (1997) explored the possibility that PSV studies may be strongly biased by the quality of the data used, concluding that the resulting dispersion was at least partly due to the incorporation of lower-quality data. Additionally, the use of sampling site paleolatitude during the conversion process of magnetic directions into VGPs causes any latitudinal independent within-site dispersion of directions to result in latitudinal dependent VGPs (Biggin et al., 2008). This is mitigated by an inbuilt correction to the conversion process but, in order for it to be effective, n must be sufficiently large so that k is a good estimate of its true value (Biggin et al., 2008). In order to assess the robustness of the resulting VGP distribution, and the influence of data quality, further selection criteria have been applied to produce a second, higher quality database. These selection criteria have been chosen as they mitigate bias associated with low n and/or k values (Biggin et al., 2008).

9. ChRM site-mean directions used must have an associated estimated Fisher concentration parameter of at least 50 ($k \geq 50$).
10. Each site-mean direction is calculated from the ChRM of a minimum of five independent samples ($n \geq 5$).

The resulting datasets from the application of selection criteria 1–8 are termed Group 1 and where selection criteria 1–10 have been applied the datasets are termed Group 2. Group 2 datasets have been analyzed in an identical process to those from Group 1 to ensure that a direct comparison of results is possible.

2.3. Measuring PSV

PSV is a measure of the variability of all of the geomagnetic field's observables; the most common way in which it is measured and assessed is by analyzing VGP dispersion (Hulot & Gallet, 1996). This VGP dispersion, otherwise known as angular dispersion, is calculated using the following equation (Cox, 1970)

$$S^2 = \frac{1}{N-1}\sum_{i=1}^{N}\Delta_i^2 \tag{1}$$

where S is the angular dispersion, N is the total number of VGPs in a given data set, and Δ_i is the angular deviation of the ith pole from the mean paleomagnetic pole, in this case the mean VGP of the data set.

The calculated VGP dispersion is the result of dispersion from two sources: a minor contribution from within-site dispersion, S_W, and a major contribution from between-site dispersion, S_B. S_W is the result of measurement errors and variations in the initial recording of the field. S_B is the dispersion between VGPs calculated from measurements at different sites due to the recording of a different field. S_B, therefore, is a measure of PSV and can be extracted by removing the contribution of S_W using the following equation

$${S_B}^2 = S^2 - \frac{{S_w}^2}{n}. \tag{2}$$

In order to calculate S_W, an estimate of the precision parameter in pole space, K, is required. This is achieved by translating k, from directional space, under the reasonable assumption that the VGP distribution is Fisherian in nature.

$$K = k\left[\frac{1}{8}\left(5 + 18\sin^2\lambda + 9\sin^4\lambda\right)\right]^{-1} \tag{3}$$

Finally, S_W is approximated by the following equation

$$S_W \cong \frac{81}{\sqrt{K}} \tag{4}$$

and the contribution of within-site dispersion can be removed using Equation 2 isolating the VGP dispersion due to PSV. This process is carried out individually for each data set in order to obtain an estimate of the dispersion associated with the PSV. This study used a non-parametric bootstrap in order to obtain 95% uncertainty estimates for S_B.

When conducting a study into VGP dispersion, it is desirable to remove VGPs that are likely to have resulted from excursional or transitional behavior. The identification and removal of outlying VGPs is done in accordance with a cut-off angle. VGPs calculated using data from a time where the field was undergoing normal secular variation tend to cluster around a mean VGP, fit by a Fisherian distribution. Any VGPs lying farther from this mean VGP than the cut-off angle are deemed to be outliers and excluded. This separation between normal secular variation and that attributed to reversals is not grounded in a fundamental understanding of the physical system; reversals and excursions are probably natural outgrowths of normal secular variation. As measurements of S_B are strongly influenced by these outlying VGPs, however, and because the time that the field spends in such states is relatively short, they are removed. Moreover, it has been shown to be an effective approach to assessing characteristics of PSV produced by numerical dynamo simulations (Biggin et al., 2020). This study applies a variable cut-off (Vandamme, 1994), calculating the optimum $\Delta_{\max}$ for the VGPs of a given data set using the following equation

$$\Delta_{\max} = 1.8S + 5. \tag{5}$$

Following the approach of Biggin et al. (2008) this study opts to use average magnetic latitude calculated from the angular distance between the mean VGP and the sampling site, rather than geographic paleolatitude. The latter would require the use of plate reconstructions which would require some circular reasoning as they are often largely based on paleomagnetic studies (Biggin et al., 2008).

2.4. Modeling VGP Dispersion

For ease of comparison with the results of previous studies (de Oliveira et al., 2018; Doubrovine et al., 2019), Model G (McFadden et al., 1988) has been used to parameterize the latitudinal dependence of PSV. It is widely accepted as a useful but imperfect descriptive tool (Doubrovine et al., 2019) and also has predictive power in determining the average axial dipole dominance of the ancient field (Biggin et al., 2020). Model G is described by the following equation

$$S_B = \sqrt{a^2 + (b\lambda)^2} \tag{6}$$

where a and b are known as the Model G shape parameters. These shape parameters have been determined by carrying out a least-squares fit between the estimated dispersion values and the model, and uncertainties in these coefficients were estimated using a jack-knife technique as carried out by McFadden et al. (1988).

3. Results

3.1. Datasets

The datasets that satisfied the Group 1 selection criteria for the Post-PCRS and PCRS time intervals are listed in Table 1. The corresponding site-level information is available in Data Sets S1 and S2. Table 1 provides background information regarding the lithology and rock units sampled, the source study, and country of origin. Most of the estimated ages presented for the Post-PCRS are the result of radiometric investigations; this is often not the case for the final PCRS datasets. Where there is no assigned numerical age, the age estimate was considered sufficient for the purpose of this study so long as the formation could be confidently attributed to the time interval in question. Within each data set, the site co-ordinates associated with the site-mean directional information have been used; however, when this was not possible, the mean site location was attributed. In either case average site co-ordinates are contained within Table 1 and displayed in Figure 1 along with the corresponding site identification code.

Also presented in Table 1 are the Van der Voo (1990) quality ratings assigned to each data set, breakdowns of which can be found in Data Set S3, the number of site-mean directions/VGPs, and the total number of samples per data set.

Data that passed the two additional selection criteria (9 & 10) are presented in Table 2 for both the Post-PCRS and PCRS. This table provides the same information regarding the datasets as in Table 1 and is presented in the same format. For both time intervals there is a reduction in the number of datasets compared with the Group 1 results, as removal of site-mean data resulted in some datasets failing criteria 4 ($N \geq 9$). The reduction of site-mean data is displayed visually in Figure 2 with sites grouped according to their associated geological epoch. Overall the amount of site-level data decreases by about one-third after Group 2 selection criteria are applied (Figure 2).

Figure 2 also displays the ages of the studied and discussed reversal regimes, defined by their average polarity reversal rate which is represented by an accompanying reversal frequency model. The reversal frequency model was constructed using a 5 Ma sliding window and magnetostratigraphic data from Ogg (2012), with the exception of 200–250 Ma where the updated GPTS of Maron et al. (2019) has been used.

Both the Post-PCRS and PCRS databases display too great a hemispherical bias to make a formal assessment of equatorial symmetry. Since the available data did not support any significant asymmetry however, we decided to display VGP dispersions on one-hemisphere projections (Figures 3 and 4).

Geochemistry, Geophysics, Geosystems

10.1029/2021GC009930

Table 1
Post-PCRS and PCRS Group 1 Datasets

Site ID	Rock formation	Country	Lithology	Rock type	Lat (°N)	Long (°E)	Age (Ma)	N	n_{tot}	Q	Plat (°N)	S_B (°)	References
PT01	Qiangtang Block middle Triassic lavas	China	Basalt	Lava flow and volcanic breccia	33.5	92.0	241	28	219	5	23.6	12.6 + 2.1/−1.9	Song et al. (2020)
PT02	Norilsk Region Volcanics	Russia	Basalt	Lava flow	70.1	94.3	251	241	2,039	5	61.0	25.2 + 1.6/−1.8	Gurevitch et al. (2004), Pavlov et al. (2007, 2019)
PT03	Los Menucos acidic dykes	Argentina	Rhyolite	Dyke	−40.4	291.6	244	12	90	5	−38.8	14.3 + 5.1/−6.2	Luppo et al. (2019)
PT04	Gezira and Bir Umhebal dyke complex	Egypt	Syenite	Dyke	23.5	33.4	226	20	88	5	19.9	16.1 + 3.6/−4.2	Lotfy and Elaal (2018)
PT05	Alto Paraguay Province	Paraguay	Syenite	Dyke	−23.5	302.1	241	10	35	5	−34.1	24.9 + 7.1/−8.2	Ernesto et al. (2015)
PT06	Tasguint and Alezmi formations	Morocco	Basalt	Lava flow	30.7	351.8	200	13	93	4	20.3	11.4 + 2.6/−3.2	Ruiz-Martinez et al. (2012)
PT07	Zguid and Ighrem dykes	Morocco	Dolerite	Dyke	30.1	352.4	200	22	181	4	23.9	10.6 + 2.9/−2.7	Palencia-Ortas et al. (2011)
PT08	Ukranian Shield andesites	Ukraine	Andesite	Dyke	47.5	37.7	204	12	80	6	46.6	11.4 + 2.9/−3.4	Yuan et al. (2011)
PT09	Puesto Viejo Group	Argentina	Basalt and rhyolite	Lava flow and ignimbrite	−34.8	291.5	245	40	332	3	−42.5	14.8 + 2.5/−2.7	Domeier, Van der Voo, Tomezzoli, et al. (2011), Valencio et al. (1975)
PT10	South Taimyr igneous complex intrusives	Russia	Dolerite	Sill	74.8	100.6	228	11	82	5	61.0	8.1 + 2.1/−2.7	Walderhaug et al. (2005)
PT11	South Taimyr igneous complex extrusives	Russia	Basalt	Lava flow	74.9	100.5	248	10	63	6	68.3	22.3 + 7.0/−10.0	Walderhaug et al. (2005)
PT12	CAMP volcanics	Morocco	Basalt	Lava flow	31.1	7.4	200	63	458	4	24.9	20.3 + 2.2/−2.4	Knight et al. (2004)
PT13	Semeitau igneous series extrusives	Kazakhstan	Basalt, rhyolite and trachyte	Lava flow and ignimbrite	50.1	79.6	248	12	150	5	45.4	12.0 + 1.8/−2.5	Lyons et al. (2002)
PT14	Issaldain and Ait-Aadel dolerites	Morocco	Basalt	Lava flow	31.5	352.8	Middle Triassic	15	72	3	23.6	14.3 + 3.0/−3.5	Hailwood (1975)

Geochemistry, Geophysics, Geosystems

10.1029/2021GC009930

Table 1
Continued

Site ID	Rock formation	Country	Lithology	Rock type	Lat (°N)	Long (°E)	Age (Ma)	N	n_{tot}	Q	Plat (°N)	S_B (°)	References
PT15	Dolomites Volcanics	Italy	Basalt	Pillow lava	46.4	11.7	238	10	51	3	16.3	15.2 + 3.0/−3.6	Manzoni (1970)
PT16	Niuhetang Formation	China	Basalt	Lava flow	23.8	99.3	Late Triassic	16	139	4	14.6	12.7 + 3.8/−3.5	Zhao et al. (2015)
PT17	Tunguska Basin intrusives	Russia	Dolerite	Dyke and sill	64.0	103.4	251	76	663	5	72.1	14.1 + 2.0/−2.0	Konstantinov et al. (2014), Latyshev et al. (2018)
PT18	Angara-Tasevva intrusives	Russia	Dolerite	Dyke and sill	56.1	99.8	251	42	431	4	57.1	15.6 + 1.9/−2.0	Latyshev et al. (2018)
PT19	East Siberian Traps	Russia	Basalt	Lava flow	66.1	111.6	250	24	118	5	62.7	17.0 + 2.1/−2.4	Kravchinsky et al. (2002)
PT20	Sierra Chica complex	Argentina	Trachyandesite and rhyolite	Pyroclastic flow and lava flow	−38.0	294.5	263	40	246	5	−40.7	11.9 + 2.4/−2.5	Domeier, Van der Voo, Tohver, et al. (2011), Tomezzoli et al. (2009)
PT21	Upper Choiyoi Group	Argentina	Rhyolite	Ignimbrite, breccia, and tuff	−34.8	291.5	264	41	272	6	−47.5	12.2 + 2.1/−2.3	Domeier, Van der Voo, Tomezzoli, et al. (2011)
K01	Bakaly formation	Kazakhstan	Basalt and basaltic andesite	Lava flow	47.5	80.7	286.3	88	502	4	37.1	9.6 + 1.5/−2.5	Bazhenov et al. (2016)
K02	Koldar formation	Kazakhstan	Dacite and rhyolite	Welded tuff and ignimbrite	47.5	80.0	306–273	15	67	4	32.2	12.7 + 2.6/−3.4	Abrajevitch et al. (2008)
K03	Lunner dykes	Norway	Larvikite and syenite	Dyke	60.3	10.5	271	37	267	3	23.0	5.6 + 1.2/−1.2	Dominguez et al. (2011)
K04	Vestfold Volcanic Plateau	Norway	Basalt	Lava flow	59.5	10.3	292	48	302	4	20.2	9.3 + 1.5/−1.5	Haldan et al. (2014)
K05	Krokskogen Volcanic Plateau	Norway	Basalt	Lava flow	60.0	10.3	284	55	384	4	23.0	9.7 + 1.5/−1.6	Haldan et al. (2014)
K06	Ukranian Shield trachytes	Ukraine	Trachyte	Dyke	47.3	37.8	282.6	19	108	4	12.8	12.4 + 2.2/−2.1	Yuan et al. (2011)
K07	Woniusi formation	China	Basalt	Lava flow	25.2	99.3	Late Carboniferous	13	65	5	42.6	17.4 + 2.4/−2.3	Huang and Opdyke (1991)
K08	Punta del Agua formation	Argentina	Andesite and lapillite	Lava flow and volcaniclastic	−28.6	291.4	Late Carboniferous	15	79	3	−48.1	16.6 + 6.1/−7.7	Geuna and Ecosteguy (2004)
K09	New England orogen	Australia	Andesite, rhyolite, and dacite	Lava flow and ignimbrite	−30.8	150.5	321–306	49	248	5	−62.8	26.2 + 3.3/−3.3	Opdyke et al. (2000)
K10	Gerringong Volcanics	Australia	Basalt - andesite	Lava flow	−34.5	150.9	265	16	120	6	−66.7	19.4 + 3.6/−3.7	Belica et al. (2017)

Geochemistry, Geophysics, Geosystems

10.1029/2021GC009930

Table 1
Continued

Site ID	Rock formation	Country	Lithology	Rock type	Lat (°N)	Long (°E)	Age (Ma)	N	n_{tot}	Q	Plat (°N)	S_B (°)	References
K11	Junggar Block dykes	China	Diabase	Dyke	45.7	82.7	Late Carboniferous	11	64	3	22.4	8.1 + 3.6/−5.5	Y. Li et al. (1989)
K12	Biyoulitie super formation	China	Basalt	Lava flow	40.7	79.7	Early Permian	20	141	5	30.7	9.6 + 2.0/−2.0	Sharps et al. (1989)
K13	Bohemian Massif	Germany	Granite-porphyry & quartzporphyry	Dyke	49.8	12.0	280	10	144	3	7.7	8.3 + 3.4/−3.6	Soffel and Harzer (1991)
K14	Sardo-Corso massif intrusives	Italy/ France	Basic	Dyke	41.1	9.3	Early Permian	23	298	3	−3.0	8.9 + 2.2/−2.5	Vigliotti et al. (1990)
K15	Esayoo formation	Canada	Basalt	Lava flow	81.0	278.0	Early Permian	12	81	4	43.5	10.8 + 3.2/−3.7	Wynne et al. (1983)
K16	Tabla formation	Chile	Rhyolite, andesite, and dacite	Lava flow and ignimbrite	−24.5	290.7	Late Carboniferous	10	30	4	−38.7	9.2 + 2.6/−3.2	Jesinkey et al. (1987)

Note. Site ID refers to an identification system used within this study, sites with codes beginning PT (Permo-Triassic) belong to the Post-PCRS database, sites with codes beginning K (Kiaman) belong to the PCRS database. Lat and Long are the mean site co-ordinates for the data set, and Age is the nominal assigned age for the data set. N is the number of site-mean directions within a data set, and n_{tot} is the total number of directions. S_B is an estimate of virtual geomagnetic pole dispersion calculated using the process set out in the method, likewise Plat is the estimated magnetic paleolatitude. "References" refer to the original studies from which the data was sourced. All of the provided information relates to site-mean directions from the referenced studies that pass Group 1 selection criteria.

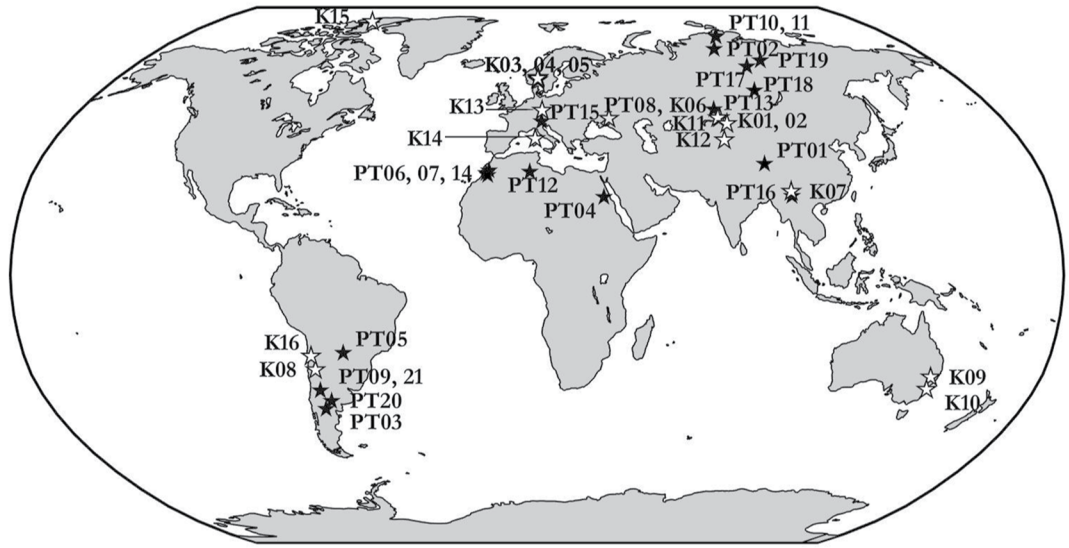

Figure 1. Sampling regions for the datasets contained in the Group 1 databases of the Post-PCRS and the Permo-Carboniferous Reversed Superchron (PCRS). Black stars represent Post-PCRS datasets, white stars represent PCRS datasets. Accompanying site identification codes are referred to in Table 1.

3.2. Post-PCRS

There is a relatively even spread of formation dates from ~200 Ma back to ~264 Ma within the Post-PCRS compilation. This is despite a moderately large number of datasets associated with the Siberian Traps and with CAMP (Table 1). Reviewing the data at the site-mean level, it is noticeable that over half of the sites representing the Post-PCRS are early Triassic in age (Figure 2). This is testament to the volume of work conducted on the Siberian Traps and the importance of this event in geological history. The mean time interval between the ages of subsequent datasets is just over 5 Ma, and the greatest time gap exists during the late Triassic where magnetic field behavior is unaccounted for about 22 Ma (Table 1). This is also the case for the late Permian for which there is no contributing data (Figure 2).

Latitudinal coverage is good with the number of low (<30°), mid- (30°–60°), and high latitudinal sites (>60°) almost evenly split, although each of these latitude bands is dominated by data from one hemisphere. Unsurprisingly, all of the high latitude datasets are related to the Siberian Traps. For low-latitude sites, the temporal range is greater, being derived from unrelated volcanic events. The mid-latitude data are primarily from South America and associated with the regional Permo-Triassic volcanism. There is also agreement in estimated dispersion values from Eurasia, however, one being late Triassic in age.

The PSV behavior appears consistent at low-mid latitudes. Figure 3a shows closely grouped VGP dispersion values for latitudes <50° lying within error of one another. Datasets from high paleolatitudes display a far less consistent dispersion pattern despite all originating from the same volcanic event. Overall, only a weak latitudinal dependence of VGP dispersion is observed; estimated dispersion values commonly lie between 10° and 15° regardless of paleolatitude.

The more robust Group 2 selection criteria remove 6 Group 1 datasets including those two with the greatest associated uncertainty of VGP dispersion (PT05 and PT11, Tables 1 and 2). From the 15 remaining datasets, just four are unaffected by the additional Group 2 selection criteria. The difference in the site-mean directional data comprising each data set does not only change the estimated values of VGP dispersion but also the estimates of paleolatitude (Tables 1 and 2).

While Group 2 data do agree better at high-latitudes, the overall observed PSV behavior of the Post-PCRS remains largely unchanged regardless of whether Group 1 or Group 2 data are used (Figure 3). The Model G a parameter decreases slightly from 14.2° (11.3°–18.1°; Group 1) to 13.3° (9.8°–18.7°; Group 2). Modeling VGP dispersion using Group 2 datasets produces an even weaker latitudinal dependence than Group 1 data-

Geochemistry, Geophysics, Geosystems

10.1029/2021GC009930

Table 2
Post-PCRS and PCRS Group 2 Datasets

Site ID	Rock formation	Country	Lithology	Rock type	Lat (°N)	Long (°E)	Age (Ma)	N	n_{tot}	Q	Plat (°N)	S_B (°)	References
PT01	Qiangtang Block middle Triassic lavas	China	Basalt	Lava flow and volcanic breccia	33.5	92.0	241	28	219	5	23.6	12.6 + 2.0/−2.0	Song et al. (2020)
PT02	Norilsk Region Volcanics	Russia	Basalt	Lava flow	70.1	94.3	251	172	1,475	5	61.2	26.2 + 2.0/−2.2	Gurevitch et al. (2004), Pavlov et al. (2007, 2019)
PT06	Tasguint and Alezmi formations	Morocco	Basalt	Lava flow	30.7	351.8	200	13	93	4	20.3	11.4 + 2.6/−3.2	Ruiz-Martinez et al. (2012)
PT07	Zguid and Ighrem dykes	Morocco	Dolerite	Dyke	30.1	352.4	200	17	150	4	23.6	9.4 + 2.5/−2.7	Palencia-Ortas et al. (2011)
PT08	Ukranian Shield andesites	Ukraine	Andesite	Dyke	47.5	37.7	204	12	80	6	46.6	11.4 + 2.9/−3.4	Yuan et al. (2011)
PT09	Puesto Viejo Group	Argentina	Basalt and rhyolite	Lava flow and ignimbrite	−34.8	291.5	245	37	313	3	−42.9	15.3 + 2.6/−2.9	Domeier, Van der Voo, Tomezzoli, et al. (2011), Valencio et al. (1975)
PT10	South Taimyr igneous complex intrusives	Russia	Dolerite	Sill	74.8	100.6	228	11	82	5	61.0	8.1 + 2.1/−2.7	Walderhaug et al. (2005)
PT12	CAMP volcanics	Morocco	Basalt	Lava flow	31.1	7.4	200	39	350	4	25.4	21.5 + 2.8/−3.0	Knight et al. (2004)
PT13	Semeitau igneous series extrusives	Kazakhstan	Basalt, rhyolite and trachyte	Lava flow and ignimbrite	50.1	79.6	248	10	77	5	45.5	12.0 + 2.3/−3.1	Lyons et al. (2002)
PT16	Niuhetang Formation	China	Basalt	Lava flow	23.8	99.3	Late Triassic	14	128	4	15.0	13.0 + 3.8/−3.4	Zhao et al. (2015)
PT17	Tunguska Basin intrusives	Russia	Dolerite	Dyke and sill	64.0	103.4	251	51	488	5	73.2	13.1 + 2.0/−2.1	Konstantinov et al. (2014), Latyshev et al. (2018)
PT18	Angara-Tasevva intrusives	Russia	Dolerite	Dyke and sill	56.1	99.8	251	34	343	4	59.4	14.7 + 1.6/−1.8	Latyshev et al. (2018)
PT19	East Siberian Traps	Russia	Basalt	Lava flow	66.1	111.6	250	10	57	5	68.0	15.0 + 4.3/−5.1	Kravchinsky et al. (2002)
PT20	Sierra Chica Complex	Argentina	Trachyandesite and rhyolite	Pyroclastic flow and lava flow	−38.0	294.5	263	28	187	5	−39.1	11.6 + 2.4/−2.5	Domeier, Van der Voo, Tohver, et al. (2011), Tomezzoli et al. (2009)
PT21	Upper Choiyoi Group	Argentina	Rhyolite	Ignimbrite, breccia, and tuff	−34.8	291.5	264	36	245	6	−47.4	12.7 + 2.2/−2.5	Domeier, Van der Voo, Tomezzoli, et al. (2011)
K01	Bakaly formation	Kazakhstan	Basalt and basaltic andesite	Lava flow	47.5	80.7	286.3	62	373	4	37.3	9.0 + 1.3/−2.5	Bazhenov et al. (2016)
K03	Lunner dykes	Norway	Larvikite and syenite	Dyke	60.3	10.5	271	26	203	3	23.6	5.5 + 1.5/−1.2	Dominguez et al. (2011)

Geochemistry, Geophysics, Geosystems

10.1029/2021GC009930

Table 2
Continued

Site ID	Rock formation	Country	Lithology	Rock type	Lat (°N)	Long (°E)	Age (Ma)	N	n_{tot}	Q	Plat (°N)	S_B (°)	References
K04	Vestfold Volcanic Plateau	Norway	Basalt	Lava flow	59.5	10.3	292	38	251	4	21.4	9.5 + 1.9/−2.0	Haldan et al. (2014)
K05	Krokskogen Volcanic Plateau	Norway	Basalt	Lava flow	60.0	10.3	284	46	334	4	22.7	10.5 + 1.7/−1.8	Haldan et al. (2014)
K06	Ukranian Shield trachytes	Ukraine	Trachyte	Dyke	47.3	37.8	282.6	10	60	4	15.6	11.6 + 2.1/−2.2	Yuan et al. (2011)
K07	Woniusi formation	China	Basalt	Lava flow	25.2	99.3	Late Carboniferous	12	61	5	42.4	18.2 + 2.0/−1.7	Huang and Opdyke (1991)
K09	New England orogen	Australia	Andesite, rhyolite, and dacite	Lava flow and ignimbrite	−30.8	150.5	321–306	28	159	5	−63.4	26.6 + 3.8/−4.0	Opdyke et al. (2000)
K10	Gerringong Volcanics	Australia	Basalt − andesite	Lava flow	−34.5	150.9	265	11	81	6	−71.8	17.5 + 3.1/−3.5	Belica et al. (2017)
K11	Junggar Block dykes	China	Diabase	Dyke	45.7	82.7	Late Carboniferous	10	60	3	22.4	8.9 + 3.5/−5.4	Y. Li et al. (1989)
K12	Biyoulitie super formation	China	Basalt	Lava flow	40.7	79.7	Early Permian	18	131	5	30.1	9.4 + 2.4/−2.4	Sharps et al. (1989)
K14	Sardo-Corso massif intrusives	Italy/ France	Basic	Dyke	41.1	9.3	Early Permian	14	138	3	−2.9	10.5 + 2.9/−3.4	Vigliotti et al. (1990)
K15	Esayoo formation	Canada	Basalt	Lava flow	81.0	278.0	Early Permian	11	75	4	43.3	10.3 + 3.6/−4.3	Wynne et al. (1983)

Note. For full description of Table 2 see note of Table 1.

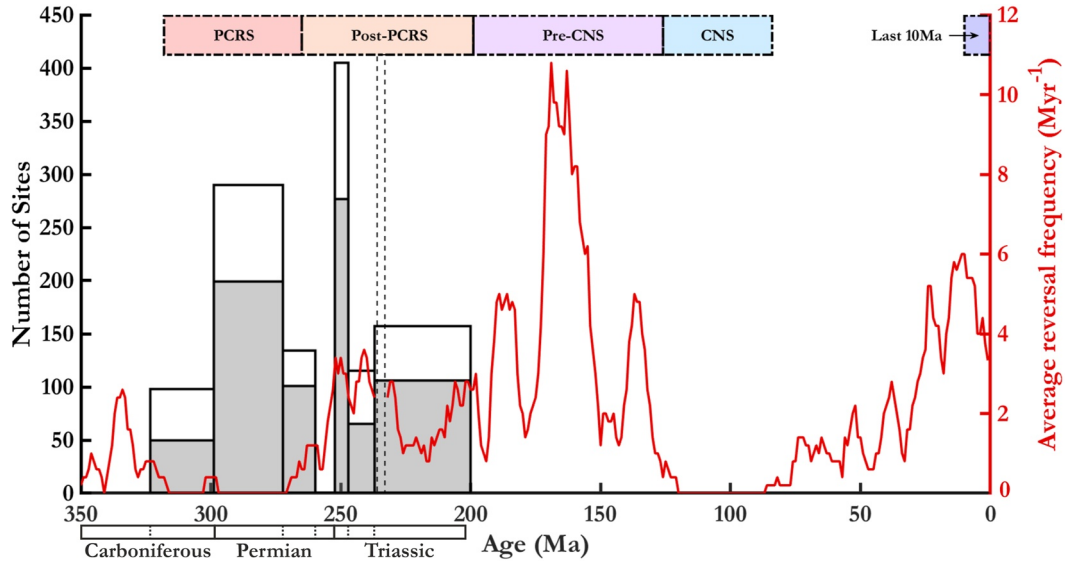

Figure 2. Graphical representation of the amount of site-level data in both the Group 1 database and the Group 2 database sub-divided by geological, epoch. The full length of the bar chart represents the amount of Group 1 data and the length of the dark gray bars represents the amount of Group 2 data. Red line displays reversal frequency model constructed using a 5 Ma sliding window and magnetostratigraphic data from Ogg (2012) and Maron et al. (2019) with the different reversal regimes studied and discussed in this study highlighted.

sets demonstrated by a slight decrease in estimated *b* value from 0.15 (0.05–0.27; Group 1) to 0.13 (0.04–0.27; Group 2).

3.3. PCRS

According to the numerical age estimates that are available, the database spans nearly all of the PCRS, starting from 265 Ma going back to at least 306 Ma. Within that time interval, coverage is consistently good through the middle and final stages of the PCRS but lacking slightly for the first few million years following its onset at ~318 Ma. The "late Carboniferous" (323.2–298.9 Ma; Davydov et al., 2012) and "early Permian" (298.9–272.3 Ma; Henderson et al., 2012) aged datasets (Table 1) are likely to have formed in and around this time interval, however, and likely ensure that the temporal representation is reasonable.

The range of latitudinal coverage is very good at low and mid- latitudes. Unlike the Post-PCRS, there is representation from very low-latitude sites (<10°). The PCRS database is lacking information at higher latitudes, however, with just two datasets above 60°. Both of these originate from Australia (Table 2) but are otherwise unrelated and separated by at least 40 Ma. Again, there is a hemispheric bias amongst the datasets with only five from 16 originating from the southern hemisphere.

Figure 4a displays a very strong relationship between VGP dispersion and latitude showing a very clear upwards trend. PSV behavior is very consistent, particularly at low-mid latitudes, but even the high latitude estimates of VGP dispersion are within error of one another. The behavior at mid-latitudes is also particularly consistent considering the seven datasets represent formations from five different countries: three from the northern hemisphere and two from the southern hemisphere.

All of the PCRS datasets are affected by the use of the Group 2 selection criteria and the subsequent removal of site-mean data; furthermore, four of the datasets are removed entirely (K02, K08, K13, K16, Tables 1 and 2). The difference between the observed dispersion patterns, when the two different sets of selection criteria were used, appears to be greater for the PCRS than for the Post- PCRS for which some datasets were unaffected. In the PCRS, estimated dispersion values are, themselves, more dispersed when Group 2 datasets are used (Figures 4a and 4b). Despite neither of the high-latitude datasets being completely removed (K09 & K10, Tables 1 and 2), the removal of site-mean data within them has altered their estimated scatter values so they are less consistent with one another (Figure 4b). Only datasets from low-latitudes display

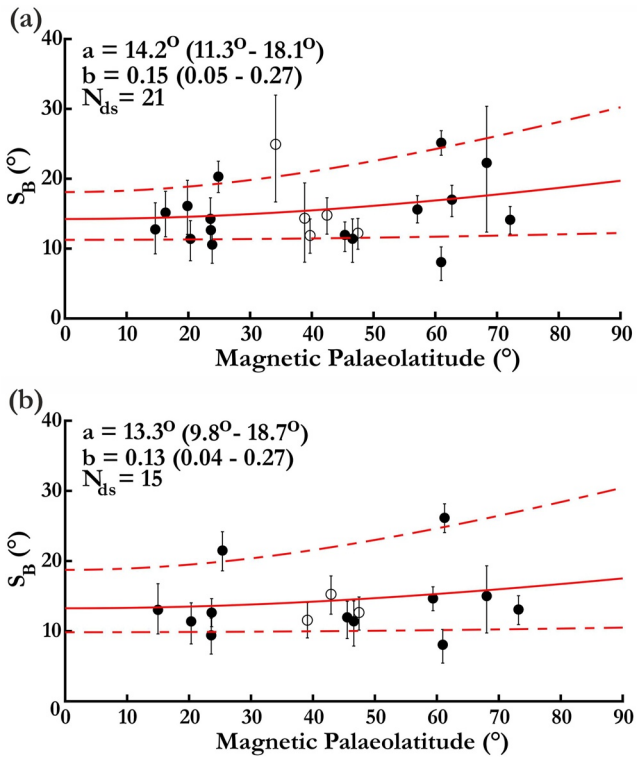

Figure 3. One hemisphere projection showing latitude dependence of virtual geomagnetic pole dispersion in the Post-PCRS (200–264 Ma). S_B values for northern and southern paleolatitudes given by filled and empty circles respectively; error bars show their 95% confidence intervals. The solid red curve displays the best fit of Model G to the S_B values, dashed line represents the 95% confidence intervals given by the jack-knife method for 5,000 replications. Estimates of Model G a and b shape parameters are displayed alongside their associated uncertainties and the number of datasets analyzed (N_{ds}). Panel (a) displays datasets after application of Group 1 selection criteria, (b) likewise for Group 2 criteria.

consistent estimates, although these have shifted, leading to an increased estimate of the Model G *a* parameter from 5.5° (0.8°–8.6°; Group 1) to 7.2° (2.0°–10.6°; Group 2). A clear trend still exists for the PCRS showing an increase in VGP dispersion with latitude, though this is slightly less well-established than in the Group 1 data as demonstrated by the increased uncertainty in estimated Model G parameters.

4. Discussion

4.1. Assessing the Robustness of VGP Dispersion

PSV analysis of the Post-PCRS paleomagnetic directional and VGP database, containing the first compilation of Triassic data, documents a S_B-λ relationship similar to those from times of claimed high reversal frequency (Biggin et al., 2008; Doubrovine et al., 2019; Franco et al., 2019). By contrast, the PCRS demonstrates a much stronger latitudinal dependence of PSV demonstrated by the estimates of Model G *b* parameter which are approximately twice those estimated for the Post-PCRS (Figures 3 and 4). The Model G *a* parameter is also substantially lower. Both of these relationships can be thought of as robust features of their respective time intervals due to the general agreement when utilizing databases of differing quality.

In the Post-PCRS, the use of higher quality Group 2 datasets reduces the estimates of both *a* and *b* relative to the Group 1 datasets.

The strong dependence of VGP dispersion with paleolatitude observed for the Group 1 PCRS datasets is in general agreement with the results of a recent study of this superchron (de Oliveira et al., 2018). The use of Group 2 datasets somewhat reduces this agreement, though not significantly. The greatest difference observed when analyzing Group 2 datasets is a rise in the Model G *a* parameter, suggesting higher dispersion at the lowest latitudes. This could be a more accurate representation of the field than that presented by Group 1 datasets but here the issue of analyzing a smaller amount of data is highlighted. The database has been reduced to 12 datasets and the removal of 1 data set at very low latitude produces an estimate of the Model G *a* parameter which is much less well constrained by the paleomagnetic data.

Although slight differences exist between the VGP dispersions observed using either Group 1 or Group 2 datasets, which can both strengthen and weaken proposed relationships, they are not significant and there is a general agreement for both the Post-PCRS and the PCRS. The higher quality datasets were compiled in order to significantly reduce the effects of bias, and their agreement with the lower quality, more numerous databases suggest that both observed VGP dispersions are unlikely to be an artifact of small *N* or *n* (Biggin et al., 2008). This establishes the respective features of both the Post-PCRS and PCRS as robust and justifies the use of Group 1 datasets for further analysis.

4.2. Comparison With Other Time Intervals

The associated Model G shape parameters (*a*, *b*, and the *b*/*a* ratio) for the Post-PCRS and PCRS intervals have been compared with those from previously compiled databases representing different time intervals. Here, we applied the Group 1 selection criteria, and the same initial constraints and method for the modeling of VGP dispersion, to the datasets from later time periods. This produced recalculated parameters which allow for a direct comparison of results. The recalculated shape parameters are given in Table 3 alongside the associated study, the time interval that they represent, and the estimated uncertainties on each parameter.

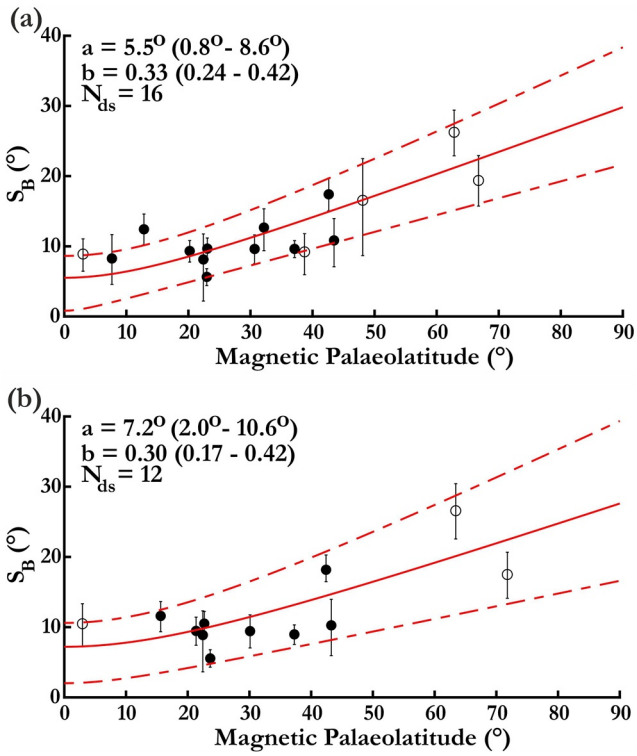

Figure 4. Latitude dependence of virtual geomagnetic pole dispersion and Model G curves for the PCRS (265–318 Ma). Panel (a) using Group 1 datasets, (b) using Group 2 datasets, see the caption of Figure 3 for description.

The time interval studied for the Post-PCRS has some crossover with the IHMP studied by Franco et al. (2019) and, as such, some of the datasets are shared. Franco et al. (2019) reported a low paleolatitudinal dependence of VGP dispersion when analyzing datasets from 265 Ma to 240 Ma, very similar to the results presented in this study for the Post-PCRS. This is further demonstrated by the similar estimates calculated for the Model G shape parameters (Table 3), suggesting consistent PSV behavior throughout the Post-PCRS.

The study of de Oliveira et al. (2018) includes sedimentary-derived data and uses less-stringent selection criteria when analyzing the PCRS. This is advantageous as more datasets are presented with increased representation at higher latitudes. The observed VGP dispersions may be compared in a similar manner to Group 1 and Group 2 datasets. There is a strong relationship between VGP dispersion and latitude with similarly low values at low latitudes presented by de Oliveira et al. (2018). This further suggests that the observed PSV behavior is a robust feature of the geomagnetic field during the PCRS.

Previous studies have used the *b/a* ratio as a way of quantifying the type of PSV behavior across a given time interval and have explored the possibility of a correlation with mean reversal frequency (de Oliveira et al., 2018; Doubrovine et al., 2019; Franco et al., 2019; McFadden et al., 1991). Figure 5a plots the *b/a* ratio values for the recalculated CNS and Pre-CNS intervals (Doubrovine et al., 2019), the PCRS and Post-PCRS intervals (this study), and a combined database for the Post-PCRS and Pre-CNS. Model G shape parameters have also been recalculated and plotted for the PSV10 database of Cromwell et al. (2018). All databases are of equal quality and represent the highest quality studies from 318 Ma to the present. Plotted alongside this is the same reversal frequency model previously presented in Figure 2.

Immediately obvious is the consistent *b/a* value throughout the Post-PCRS and the Pre-CNS and the higher values associated with the superchrons on either side (Figure 5a). During the newly combined interval, reversal frequency shows a wide range of values (Figure 5a) which would appear to contradict the idea that an inverse relationship exists between the *b/a* ratio and reversal frequency (Franco et al., 2019).

Table 3
Comparison of Model G Shape Parameters and Axial Dipole Dominance Recalculated Using Our Selection Criteria Applied to the Datasets Originally Selected in the Studies Given

Time interval	Age range (Ma)	Average reversal frequency (Myr^{-1})	a (°)	b	b/a	AD/NAD_{median}	Study
Last 10 Ma	0–10	4.9	12.0 + 3.3/−1.9	0.27 + 0.04/−0.07	0.022 ± 0.0066	10.0 + 18.9/−7.2	1
CNS	84–126	0.095	10.0 + 2.1/−2.8	0.22 + 0.05/−0.10	0.022 ± 0.012	15.1 + 29.9/−10.2	2
Pre-CNS	126–198	4.2	12.7 + 2.6/−2.4	0.13 + 0.13/−0.09	0.010 ± 0.0075	8.8 + 18.9/−6.0	2
Post-PCRS	200–264	2.0	14.2 + 3.9/−0.9	0.15 + 0.12/−0.10	0.011 ± 0.0073	6.9 + 9.2/−5.0	3
Pre-CNS and Post-PCRS	126–264	3.1	13.3 + 2.3/−2.1	0.15 + 0.10/−0.10	0.012 ± 0.0083	7.9 + 15.2/−5.3	3
PCRS	265–318	0.076	5.5 + 3.1/−4.7	0.33 + 0.09/−0.09	0.059 ± 0.052	58.4 + 6345.1/−47.3	3
IHMP	*240–265*	*2.2*	*12.3 + 20.7/−7.2*	*0.10 + 0.08/−0.05*	*0.0083 ± 0.0066*	*9.5 + 114.3/−9.1*	*4*
PCRS	*265–318*	*0.076*	*4.1 + 3.2/−4.0*	*0.32 + 0.14/−0.12*	*0.078 ± 0.080*	*113.5 ± −*	*5*

Note. AD/NAD_{median} is the estimation of the ratio of non-axial dipole field to axial dipole field (Biggin et al., 2020) with the associated uncertainty limits where reasonable. Italicized parameters are associated with time intervals that were the subject of previous studies and contain data which has been incorporated into either the Post-PCRS or PCRS database of this study. References: [1] Cromwell et al. (2018), [2] Doubrovine et al. (2019), [3] This study, [4] Franco et al. (2019), [5] de Oliveira et al. (2018).

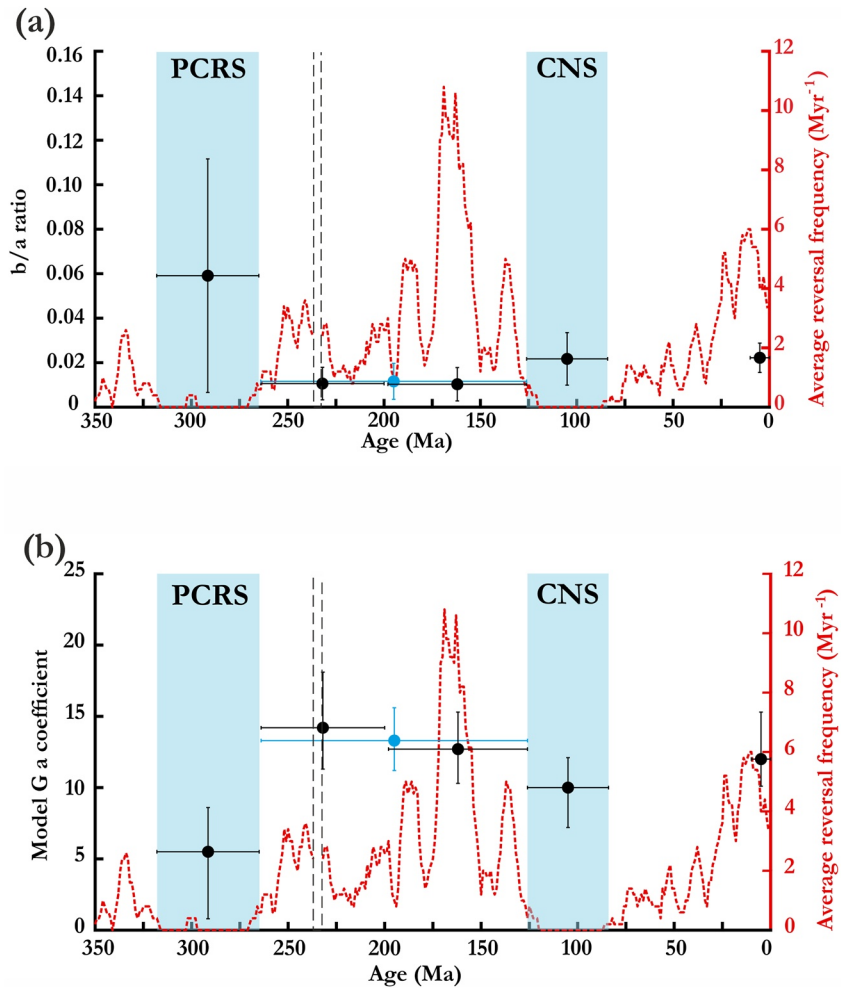

Figure 5. Variations in (a) Model G b/a ratio (b) Model G a parameter estimated for a range of time intervals. Last 10 Ma (0–10 Ma), (CNS (84–126 Ma), Pre-CNS (126–198 Ma), Post-PCRS (200–246 Ma), Pre-CNS and Post-PCRS (126–264 Ma), PCRS (265–318 Ma)). CNS and Pre-CNS data taken from Doubrovine et al. (2019), last 10 Ma data taken from Cromwell et al. (2018). Estimates of (a) b/a ratio and (b) Model G a parameter given by solid circles, vertical error bars represent the 95% confidence interval, horizontal error bars represent age range. The results displayed in blue are those from the combined database for the Post-PCRS and Pre-CNS. Dashed red line displays reversal frequency model constructed using a 5 Ma sliding window and magnetostratigraphic data from Ogg (2012) and Maron et al. (2019).

Rather, it supports the hypothesis that any potential relationship must be less straightforward (Doubrovine et al., 2019). The stronger latitudinal dependence of dispersion (i.e., the Model G *b* parameter) during both the PCRS (Figure 5a) and CNS (Doubrovine et al., 2019) are responsible for the higher *b/a* ratio compared to the times of geomagnetic reversals. This could suggest that the different behaviors are indicative of a low/absent reversal regime and one in which reversals are present. However, the indistinguishable *b/a* ratio for the last 10 Ma, when compared to that of the CNS, is not consistent with this hypothesis (Doubrovine et al., 2019).

If the *b/a* ratio does not have a straightforward relationship with the average reversal frequency, then the consistently low value between the two superchrons must have an alternative explanation. Interestingly, there is an ongoing discussion around a proposed feature of the paleointensity record across a similar time interval, the Mesozoic Dipole Low (MDL). This feature was first proposed by Prévot et al. (1990) and was defined as a period in which the virtual dipole moment (VDM) was one third of its present-day value between ~180-135 Ma (McElhinny & Larson, 2003; Prévot et al., 1990). This hypothesis was broadly supported by the work of Tanaka et al. (1995), in their construction and analysis of a global palaeointensity database,

and low paleointensity estimates obtained from the Siberian Traps (Heunemann et al., 2004; Shcherbakova et al., 2015).

Subsequent studies have suggested an MDL ~180-120 Ma (Perrin & Shcherbakov, 1997), and recent low VDM estimates obtained from Permo-Triassic boundary rocks (~250 Ma) have led to proposals of an MDL extending back to this time (Anwar et al., 2016). The time interval corresponding to this longer MDL is largely encompassed by the time interval of low *b/a* ratios compiled for this study. Exploring this relationship further is very challenging due to the current global paleointensity record. As it stands there are almost no VDM estimates for the entirety of the Triassic (Anwar et al., 2016). Furthermore, there is the possibility that the MDL is not a time interval of low intensity but rather represents the long-term average (Selkin & Tauxe, 2000). Another possibility is that the real MDL is a time of low field strength associated solely with the Jurassic hyperactivity period (Kulakov et al., 2019).

Obtaining new estimates of absolute paleointensity values during the Triassic will be crucial in making possible the assessment of any relationships between geomagnetic observables and the paleointensity record. The compilation of data from Triassic aged volcanic rocks and small-scale intrusions in Table 1 demonstrates that this is possible as such rock formations have the potential to be viable paleointensity recorders. The number of Group 1 datasets available per million year for Triassic PSV analysis (0.23 Myr^{-1}) is not substantially lower than other time intervals (e.g., CNS; 0.45 Myr-1, Pre-CNS; 0.26 Myr^{-1}; Doubrovine et al., 2019, PCRS 0.30 Myr^{-1}; this study) even after removing datasets associated with the two major volcanic events that bookend the period. Due to the nature of paleointensity experiments (Shaar & Tauxe, 2015; Thellier & Thellier, 1959) some formations that are suitable for paleomagnetic studies are not suitable for paleointensity studies, however. Nevertheless, we highlight the potential for future work to characterize the Triassic dipole moment using paleointensity studies performed on such targets as identified in Table 1.

4.3. Implications for Field Morphology

A recent study by Biggin et al. (2020) investigated, across a wide range of models, the possibility of using Model G shape parameters to provide information about field morphology and, specifically, the dominance of the axial dipole contribution. Their finding was a strong, positive relationship between axial dipole dominance and the Model G *a* parameter. In order to assess what this would mean for the time intervals considered in this study, the different estimated *a* values must be analyzed in a similar manner to that done for the *b/a* ratios (Figure 5b). The relationship between estimated *a* values and apparent average reversal frequency does not appear to be strongly inverse to that observed when analyzing the *b/a* ratio (Figure 5), as would be expected if the parameters co-varied inversely. The superchrons do display the lowest *a* values alongside higher estimated *b* values. Nevertheless, the estimated *a* value for the last 10 Ma is more comparable to that observed during the Pre-CNS, despite the associated estimated *b* value more closely resembling those of the two superchrons (Table 3). This would appear to support the conclusion of Biggin et al. (2020) that only a weak relationship exists between Model G shape parameters. The consequence of a relationship of this nature is that the original interpretation of the Model G shape parameters, as representing independent families of equatorially symmetric and equatorially anti-symmetric terms (McFadden et al., 1988, 1991), is not well- supported (Biggin et al., 2020). A similar conclusion regarding the physical meaning of Model G shape parameters was reached by Doubrovine et al. (2019) who suggested that in strong-field, Earth-like dynamos the separation between the symmetric and anti-symmetric dynamo families becomes improbable despite being theoretically plausible.

Estimates of the Model G *a* parameter were used to establish the relative contribution of the axial dipole using the power law established by Biggin et al. (2020). The output is the median ratio of axial dipole to non-axial dipole contribution across the time interval (AD/NAD_{median}), with the median being used to avoid biasing due to brief, extreme events. The estimated ratios are displayed in Table 3. For the PCRS and Post PCRS, it is the first time that the field behavior has been analyzed in this way. The relative contribution of the axial dipole component of the field is somewhat similar for the Post-PCRS and Pre-CNS (Table 3) although a small increase is observed. Axial dipole dominance has since decreased, with the field over the last 10 Ma demonstrating a relative dipole contribution level similar to that during the Pre-CNS (Table 3). The most remarkable finding is the very strong axial dipole dominance of the PCRS field (Table 3), which is far greater than for any of the other ancient time intervals studied here or by Biggin et al. (2020). The

closest values to this have come from much more recent, shorter time intervals on the order of 10 kyr (Biggin et al., 2020). The enhanced axial dipole dominance of the PCRS suggests that the Earth's magnetic field, during time instances within this interval, more closely resembled that of a GAD field than during any other time interval comparably studied. Put another way, dipole tilt (produced by the equatorial dipole terms) and all components of the nondipole field appear to have been heavily diminished relative to the axial dipole term during much of the PCRS. This offers a possible explanation for the enhanced duration of the PCRS, when compared to that of the CNS. Since collapse of the axial dipole is required to trigger a reversal (e.g., Olson et al., 2009), it being stronger and more dominant through most of the time interval would reduce the number of opportunities for a transitional field to dominate. The estimate of AD/NAD_{median} for the PCRS is a factor of 5 larger than the estimates for the other intervals since 265 Ma, with the upper range essentially describing a pure GAD field (Table 3). Associated uncertainty estimates for AD/NAD_{median} are inflated through incorporation of uncertainties associated with both the Model G *a* parameter and the power law fit of Biggin et al. (2020) that relates this to AD/NAD_{median}. Nevertheless, these uncertainty bounds still only narrowly incorporate the AD/NAD_{median} for the CNS and exclude the estimates for all intervals during which magnetic polarity reversals takes place. Therefore, although the formal establishment of the axial dipole dominance of the PCRS as statistically distinct from that of all other intervals must await the addition of further PSV data, we nevertheless consider it likely that, during the PCRS, the field was on average more axially dipolar field than at any subsequent time.

The possible relationships between axial dipole dominance and VDM can be illustrated as two end-member scenarios with a spectrum between. In the first, the non-axial dipole field remains approximately constant through time with changes in the VDM being entirely accounted for by shifts in the median axial dipole component. In the second, all components of the field vary in unison. Our new findings regarding the PCRS appear to rule out the second scenario (since the axial dipole does appear to have been enhanced at the expense of the rest of the field during this time). The observation that average VDM also appears to have been elevated during the PCRS (Hawkins et al., 2021) rather supports the first scenario, or somewhere on the spectrum near to it. Likewise, if the duration of the MDL was shown to coincide with the time interval represented by the combined Pre-CNS and Post-PCRS then this could suggest that an increased contribution from the non-axial dipole field was a factor in the lower average VDM.

5. Conclusions

PSV behavior during the Post-PCRS is very similar to that observed for the Pre-CNS despite these two intervals being characterized by different mean reversal rates. In terms of their PSV behavior, we suggest that they can adequately be represented as a single interval. The variable reversal frequency and consistent *b/a* ratio is not consistent with the hypothesis that an inverse relationship exists between the two (Franco et al., 2019). This observation is further demonstrated by the indistinguishable estimates of *b/a* ratio for the CNS and the last 10 Ma (Doubrovine et al., 2019). Detailed analysis of PSV behavior during the Jurassic hyperactivity period could help reveal whether PSV behavior was, indeed, consistent throughout the Post-PCRS and Pre-CNS, and contribute to the ongoing discussion surrounding the nature of the relationship between VGP dispersion and reversal frequency. In order to conduct such a study, more high quality VGP datasets representing Jurassic hyperactivity behavior are required than are currently available.

It would appear that the original interpretation of Model G shape parameters in terms of competing and co-varying contributions from quadrupole and dipole family harmonic terms (McFadden et al., 1988, 1991) is not appropriate. Over at least the last 318 Ma, superchrons seem to be characterized by a lower *a* parameter, which can likely be attributed to a more axial dipole dominated field (Biggin et al., 2020). This enhanced dipole dominance suppresses dipole tilt and the nondipole field, in turn suppressing VGP dispersion and the frequency of reversals. It appears that this behavior was much more enhanced during the PCRS, in contrast to previous comparisons that have argued for similar PSV behavior in the CNS and PCRS (de Oliveira et al., 2018; Haldan et al., 2014). The enhanced dipole dominance could go towards explaining the apparent longer duration of the superchron. It is also possible that the MDL is characterized by near latitudinal invariance of VGP dispersion and partially reduced axial dipole dominance as attested to by the marginally higher Model G *a* parameter. Testing this hypothesis will require a much greater insight into global dipole moment variability, in particular for the Triassic, in order to better constraint the extent of the

MDL. Considering the viability of the formations in Table 1 as potential targets for future paleointensity studies would be a good first step towards addressing some of the gaps in the VDM record.

The low VGP dispersion at low-latitudes and the strong latitudinal dependence of VGP dispersion previously observed for the PCRS (de Oliveira et al., 2018) is a robust feature, demonstrated by the similarity in the pattern observed in this study using a higher-quality database. This behavior is distinguishable from that observed during the Pre-CNS and Post-PCRS and is the most extreme example of latitudinal-dependent VGP dispersion. This would suggest that the PCRS occurred during a time interval in which the Earth's magnetic field was greatly dipole dominated, and potentially of high intensity, making it a time interval worthy of intensive future study.

Data Availability Statement

The original datasets compiled for this research are available through EarthRef Digital Archive (https://earthref.org/ERDA/2481, ERDA), and are also provided in the Supporting Information S1. A complete breakdown of the Supporting Information is available in "Supporting Information S1." Previously compiled data are available through their respective publications, Cromwell et al. (2018) (PSV10), and Doubrovine et al. (2019) (CNS and Pre-CNS).

Acknowledgments
This research was the result of funding from The Leverhulme Trust (Research Leadership Award, RLA-2016-080), the Natural Environment Research Council (NE/T012463/1), and the Netherlands Organisation for Scientific Research (NWO). The additional PCRS data used in this study were compiled by Marcela Haldan at Utrecht University with funding from the NWO.

References

Abrajevitch, A., Van der Voo, R., Bazhenov, M. L., Levashova, N. M., & McCausland, P. J. A. (2008). The role of Kazakhstan orocline in the late Paleozoic amalgamation of Eurasia. *Tectonophysics*, *455*, 61–76. https://doi.org/10.1016/j.tecto.2008.05.006

Anwar, T., Hawkins, L., Kravchinsky, V. A., Biggin, A. J., & Pavlov, V. E. (2016). Microwave paleointensities indicate a low paleomagnetic dipole moment at Permo-Triassic boundary. *Physics of the Earth and Planetary Interiors*, *260*, 62–73. https://doi.org/10.1016/j.pepi.2016.09.007

Bazhenov, M. L., Van der Voo, R., Menzo, Z., Dominguez, A. R., Meert, J. G., & Levashova, N. M. (2016). Paleomagnetism and dating of a thick lava pile in the Permina Bakaly formation of eastern Kazakhstan: Regularities and singularities of the paleomagnetic record in thick lava series. *Physics of the Earth and Planetary Interiors*, *253*, 5–20. https://doi.org/10.1016/j.pepi.2016.02.001

Belica, M. E., Tohver, E., Pisarevsky, S. A., Jourdan, F., Denyszyn, S., & George, A. D. (2017). Middle Permian paleomagnetism of the Sydney Basin, Eastern Gondwana: Testing Pangea models and the timing of the end of the Kiaman Reverse Superchron. *Tectonophysics*, *699*, 178–198. https://doi.org/10.1016/j.tecto.2016.12.029

Benton, M. J. (2016). The Triassic. *Current Biology*, *26*, R1205–R1218. https://doi.org/10.1016/j.cub.2016.10.060

Biggin, A. J., Bono, R., Meduri, D. G., Sprain, C., Davies, C., Holme, R., & Doubrovine, P. V. (2020). Quantitative estimates of average geomagnetic axial dipole dominance in deep geological time. *Nature Communications*, *11*, 6100. https://doi.org/10.1038/s41467-020-19794-7

Biggin, A. J., Steinberger, B., Aubert, J., Suttie, N., Holme, R., Torsvik, T. H., et al. (2012). Possible links between long-term geomagnetic variations and whole-mantle convection processes. *Nature Geoscience*, *5*, 526–533. https://doi.org/10.1038/ngeo1521

Biggin, A. J., van Hinsbergen, D. J. J., Langereis, C. G., Straathof, G. B., & Deenen, M. H. L. (2008). Geomagnetic secular variation in the Cretaceous Normal Superchron and in the Jurassic. *Physics of the Earth and Planetary Interiors*, *169*(1–4), 3–19. https://doi.org/10.1016/j.pepi.2008.07.004

Bleeker, W. (2004). Towards a 'natural' time scale for the Precambrian – A proposal. In F. M. Gradstein, J. G. Ogg, & A. G. Smith (Eds.), *A geologic time scale* (pp. 141–146). Cambridge University Press. https://doi.org/10.1017/CBO9780511536045

Burgess, S. D., Muirhead, J. D., & Bowring, S. A. (2017). Initial pulse of Siberian Traps sills as the trigger of the end-Permian mass extinction. *Nature Communications*, *8*, 164. https://doi.org/10.1038/s41467-017-00083-9

Cox, A. (1970). Latitude dependence of the angular dispersion of the geomagnetic field. *Geophysical Journal of the Royal Astronomical Society*, *20*(3), 253–269. https://doi.org/10.1111/j.1365-246X.1970.tb06069.x

Cromwell, G., Johnson, C. L., Tauxe, L., Constable, C. G., & Jarboe, N. A. (2018). PSV10: A global dataset for 0–10 Ma time-averaged field and paleosecular variation studies. *Geochemistry, Geophysics, Geosystems*, *19*, 1533–1558. https://doi.org/10.1002/2017GC007318

Davydov, V. I., Korn, D., Schmitz, M. D., Gradstein, F. M., & Hammer, O. (2012). The Carboniferous period. In F. M. Gradstein, J. G. Ogg, M. D. Schmitz, & G. M. Ogg (Eds.), *The geologic time scale* (pp. 603–651). Elsevier. https://doi.org/10.1016/B978-0-444-59425-9.00023-8

de Oliveira, W. P., Franco, D. R., Brandt, D., Ernesto, M., da Ponte Neto, C. F., Zhao, X., et al. (2018). Behaviour of the paleosecular variation during the Permian-Carboniferous reversed superchron and comparisons to the low reversal frequency intervals since Precambrian times. *Geochemistry, Geophysics, Geosystems*, *19*, 1035–1048. https://doi.org/10.1002/2017GC007262

Domeier, M., Van der Voo, R., Tohver, E., Tomezzoli, R. N., Vizan, H., Torsvik, T. H., & Kirshner, J. (2011). New Late Permian paleomagnetic data from Argentina: Refinement of the apparent polar wander path of Gondwana. *Geochemistry, Geophysics, Geosystems*, *12*, Q07002. https://doi.org/10.1029/2011GC003616

Domeier, M., Van der Voo, R., Tomezzoli, R. N., Tohver, E., Hendriks, B. W. H., Torsvik, T. H., et al. (2011). Support for an "A-type" Pangea reconstruction from high-fidelity Late Permian and Early to Middle Triassic paleomagnetic data. *Journal of Geophysical Research*, *116*, B12144. https://doi.org/10.1029/2011JB008495

Dominguez, A. R., Van de Voo, R., Torsvik, T. H., Hendriks, B. W. H., Abrajevitch, A., Domeier, M., et al. (2011). The ~270 Ma palaeolatitude of Baltica and its significance for Pangea models. *Geophysical Journal International*, *186*, 529–550. https://doi.org/10.1111/j.1365-246X.2011.05061.x

Donadini, F., Riisager, P., Korhonen, K., Kahma, K., Pesonen, L., & Snowball, I. (2007). Holocene geomagnetic paleointensities: A blind test of absolute paleointensity techniques and materials. *Physics of the Earth and Planetary Interiors*, *161*, 19–35. https://doi.org/10.1016/j.pepi.2006.12.002

Doubrovine, P. V., Veikkolainen, T., Pesonen, L. J., Piispa, E., Ots, S., Smirnov, A. V., et al. (2019). Latitude dependence of geomagnetic paleosecular variation and its relation to the frequency of magnetic reversals: Observations from the Cretaceous and Jurassic. *Geochemistry, Geophysics, Geosystems*, *20*, 1240–1279. https://doi.org/10.1029/2018GC007863

Ernesto, M., Comin-Chiaramonti, P., & de Barros Gomes, C. (2015). The Early Triassic magmatism of the Alto Paraguay Province, Central South America: Paleomagnetic and ASM data. *Open Geosciences*, *7*(1), 386–394. https://doi.org/10.1515/geo-2015-0022

Franco, D. R., de Oliveira, W. P., de Freitas, F. B. V., Takahashi, D., de Ponte Neto, C. S., & Peixoto, I. M. C. (2019). Paleomagnetic evidence for inverse correspondence between the relative contribution of the axial dipole field and CMB heat flux for the past 270 Myr. *Scientific Reports*, *9*, 1–8. https://doi.org/10.1038/s41598-018-36494-x

Geuna, S. E., & Ecosteguy, L. D. (2004). Palaeomagnetism of the upper carboniferous-lower Permian transition from Paganzo basin, Argentina. *Geophysical Journal International*, *157*, 1071–1089. https://doi.org/10.1111/j.1365-246X.2004.02229.x

Gubbins, D. (1987). Mechanism for geomagnetic polarity reversals. *Nature*, *326*, 167–169. https://doi.org/10.1038/326167a0

Gurevitch, E. L., Heunemann, C., Rad'ko, K., Westphal, M., Bachtadse, V., Pozzi, J. P., & Feinberg, H. (2004). Palaeomagnetism and magnetostratigraphy of the Permian-Triassic northwest central Siberian Trap Basalts. *Tectonophysics*, *379*, 211–226. https://doi.org/10.1016/j.tecto.2003.11.005

Hailwood, E. A. (1975). The palaeomagnetism of Triassic and Cretaceous rock from Morocco. *Geophysical Journal International*, *43*, 1029–1030. https://doi.org/10.1111/j.1365-246X.1975.tb04149.x

Haldan, M. M., Langereis, C. G., Biggin, A. J., Dekkers, M. J., & Evans, M. E. (2009). A comparison of detailed equatorial red bed records of secular variation during the permo-carboniferous reversed superchron. *Geophysical Journal International*, *177*, 834–848. https://doi.org/10.1111/j.1365-246X.2009.04124.x

Haldan, M. M., Meijers, M. J. M., Langereis, C. G., Larsen, B. T., & Heyer, H. (2014). New palaeomagnetic results from the Oslo Graben, a Permian Superchron lava province. *Geophysical Journal International*, *199*, 1554–1571. https://doi.org/10.1093/gji/ggu351

Haque, Z., Geissman, J. W., Irmis, R. B., Olsen, P. E., Lepre, C., Buhedma, H., et al. (2021). Magnetostratigraphy of the Triassic Moenkopi Formation from the continuous cores recovered in Colorado Plateau Coring Project Phase 1 (CPCP-1), Petrified Forest National Park, Arizona, USA: Correlation of the Early to Middle Triassic strata and biota in Colorado Plateau and its environs. *Journal of Geophysical Research: Solid Earth*, *126*(9), e2021JB021899. https://doi.org/10.1029/2021JB021899

Hawkins, M. A., Grappone, J. M., Sprain, C. J., Saengduean, P., Sage, E. J., Thomas-Cunningham, S., et al. (2021). Intensity of the Earth's magnetic field: Evidence for a Mid-Paleozoic dipole low. *Proceedings of the National Academy of Sciences of the United States of America*, *118*(34), e2017342118. https://doi.org/10.1073/pnas.2017342118

Henderson, C. M., Davydov, V. I., Wardlaw, B. R., Gradstein, F. M., & Hammer, O. (2012). The Permian period. In F. M. Gradstein, J. G. Ogg, M. D. Schmitz, & G. M. Ogg (Eds.), *The geologic time scale* (pp. 653–679). Elsevier. https://doi.org/10.1016/B978-0-444-59425-9.00024-X

Heunemann, C., Krása, D., Soffel, H. C., Gurevitch, E., & Bachtadse, V. (2004). Directions and intensities of the Earth's magnetic field during a reversal: Results from the Permo-Triassic Siberian trap basalts, Russia. *Earth and Planetary Science Letters*, *218*, 197–213. https://doi.org/10.1016/S0012-821X(03)00642-3

Hounslow, M. W., Domeier, M., & Biggin, A. J. (2018). Subduction flux modulates the geomagnetic polarity reversal rate. *Tectonophysics*, *742–743*, 34–49. https://doi.org/10.1016/j.tecto.2018.05.018

Hounslow, M. W., & Muttoni, G. (2010). The geomagnetic polarity timescale for the Triassic: Linkage to stage boundary definitions. *Geological Society, London, Special Publications*, *334*, 61–102. https://doi.org/10.1144/SP334.4

Huang, K., & Opdyke, N. D. (1991). Paleomagnetic results from the Upper Carboniferous of the Shan-Thai-Malay block of western Yunnan, China. *Tectonophysics*, *192*, 333–344. https://doi.org/10.1016/0040-1951(91)90107-4

Hulot, G., & Gallet, Y. (1996). On the interpretation of virtual geomagnetic pole (VGP) scatter curves. *Physics of the Earth and Planetary Interiors*, *95*(1–2), 37–53. https://doi.org/10.1016/0031-9201(95)03106-5

Jesinkey, C., Forsythe, R. D., Mpodozis, C., & Davidson, J. (1987). Concordant late Paleozoic paleomagnetizations from the Atacama Desert: Implications for tectonic models of the Chilean Andes. *Earth and Planetary Science Letters*, *85*, 461–472. https://doi.org/10.1016/0012-821X(87)90141-5

Johnson, C. L., & McFadden, P. (2015). The time-averaged field and paleosecular variation. In G. Schubert (Ed.), *Treatise on Geophysics* (2nd ed., Vol. 5, pp. 385–417). Elsevier. https://doi.org/10.1016/B978-0-444-53802-4.00105-6

Kent, D. V., Olsen, P. E., Lepre, C., Rasmusen, C., Mundil, R., Gehrels, G. E., et al. (2019). Magnetochronology of the entire Chinle formation (Norian age) in a scientific drill core from Petrified Forest National Park (Arizona, USA) and implications for regional and global correlations in the Late Triassic. *Geochemistry, Geophysics, Geosystems*, *20*(11), 4654–4664. https://doi.org/10.1029/2019GC008474

Kent, D. V., Olsen, P. E., & Muttoni, G. (2017). Astrochronostratigraphic polarity time scale (APTS) for the Late Triassic and Early Jurassic from continental sediments and correlation with standard marine stages. *Earth-Science Reviews*, *166*, 153–180. https://doi.org/10.1016/j.earscirev.2016.12.014

Kent, D. V., Olsen, P. E., Rasmussen, C., Lepre, C., Mundil, R., Irmis, R. B., et al. (2018). Empirical evidence for stability of the 405-kiloyear Jupiter-Venus eccentricity cycle over hundreds of millions of years. *Proceedings of the National Academy of Sciences of the United States of America*, *115*(24), 6153–6158. https://doi.org/10.1073/pnas.1800891115

Knight, K. B., Nomde, S., Renne, P. R., Marzoli, A., Bertrand, H., & Youbi, N. (2004). The Central Atlantic Magmatic Province at the Triassic-Jurassic boundary: Paleomagnetic and $^{40}Ar/^{39}Ar$ evidence from Morocco for brief, episodic volcanism. *Earth and Planetary Science Letters*, *228*, 143–160. https://doi.org/10.1016/j.epsl.2004.09.022

Konstantinov, K. M., Bazhenov, M. L., Fetisova, A. M., & Khutorskoy, M. D. (2014). Paleomagnetism of trap intrusions, East Siberia: Implications to flood basalt emplacement and the Permo-Triassic crisis of biosphere. *Earth and Planetary Science Letters*, *394*, 242–253. https://doi.org/10.1016/j.epsl.2014.03.029

Kravchinsky, V. A., Konstantinov, K. M., Courtillot, V., Savrasov, J. I., Valet, J., Cherniy, S. D., et al. (2002). Palaeomagnetism of East Siberian traps and kimberlites: Two new poles and palaeogeographic reconstructions at about 360 and 250 Ma. *Geophysical Journal International*, *148*, 1–33. https://doi.org/10.1046/j.0956-540x.2001.01548.x

Kulakov, E. V., Sprain, C. J., Doubrovine, P. V., Smirnov, A. V., Paterson, G. A., Hawkins, L., et al. (2019). Analysis of an updated paleointensity database (Q_{PI}-PINT) for 65-200 Ma: Implications for the long-term history of dipole moment through the Mesozoic. *Journal of Geophysical Research: Solid Earth*, *124*, 9999–10022. https://doi.org/10.1029/2018JB017287

Latyshev, A. V., Veselovskiy, R. V., & Ivanov, A. V. (2018). Paleomagnetism of Permian-Triassic intrusions from the Tunguska syncline and the Angara-Taseeva depression, Siberian Traps Large Igneous Province: Evidence of contrasting styles of magmatism. *Tectonophysics*, *723*, 41–55. https://doi.org/10.1016/j.tecto.2017.11.035

Lerner, G. A., Smirnov, A. V., Survitckii, L. V., & Piispa, E. J. (2017). Nonheating methods for absolute paleointensity determination: Comparison and calibration using synthetic and natural magnetite-bearing samples. *Journal of Geophysical Research: Solid Earth*, *122*, 1614–1633. https://doi.org/10.1002/2016JB013777

Li, M., Ogg, J., Zhang, Y., Huang, C., Hinnov, L., Chen, Z., & Zou, Z. (2016). Astronomical tuning of the end-Permian extinction and the Early Triassic epoch of South China and Germany. *Earth and Planetary Science Letters*, *441*, 10–25. https://doi.org/10.1016/j.epsl.2016.02.017

Li, Y., Sharps, R., McWilliams, M., Nur, A., Li, Y., Li, Q., & Zhang, W. (1989). Paleomagnetic results from Late Paleozoic dikes from the northwestern Junggar Block, northwestern China. *Earth and Planetary Science Letters*, *94*, 123–130. https://doi.org/10.1016/0012-821X(89)90088-5

Lotfy, H., & Elaal, E. A. (2015). Equatorial paleolatitude for Northeast Africa in the Late Triassic: Paleomagnetic study on the Gezira and Bir-Umhebal [229-223 Ma] ring complexes, Southeastern Desert, Egypt. *Arabian Journal of Geosciences*, *11*, 446. https://doi.org/10.1007/s12517-018-3806-x

Lucas, S. G. (2005). Pangaea. In R. C. Selley, L. R. M. Cocks, & I. R. Plimer (Eds.), *Encyclopedia of geology* (pp. 225–228). Elsevier. https://doi.org/10.1016/B0-12-369396-9/00434-2

Lucas, S. G. (2010). Multichron. *Lethaia*, *43*, 282. https://doi.org/10.1111/j.1502-3931.2009.00207.x

Lucas, S. G., & Tanner, L. H. (2014). The Triassic timescale 2013. In R. Rocha, J. Pais, J. C. Kullberg, & S. Finney (Eds.), *Strati 2013* (pp. 19–22). Springer. https://doi.org/10.1007/978-3-319-04364-7_4

Lund, S. P., & Keigwin, L. (1994). Measurement of the degree of smoothing in sediment paleomagnetic secular variation records: An example from late Quaternary deep-sea sediments of the Bermuda Rise, western North Atlantic Ocean. *Earth and Planetary Science Letters*, *122*, 317–330. https://doi.org/10.1016/0012-821X(94)90005-1

Luppo, T., Martinez Dopico, C. I., Rapalini, A. E., López de Luchi, M. G., Miguez, M., & Fanning, C. M. (2019). Paleomagnetism of Permo-Triassic volcanic units in northern Patagonia: Are we tracking the final stages of collision of Patagonia? *International Journal of Earth Sciences*, *108*, 621–647. https://doi.org/10.1007/s00531-018-01672-9

Lyons, J. J., Coe, R. S., Zhao, X., Renne, P. R., Kazansky, A. Y., Izokh, A. E., et al. (2002). Paleomagnetism of the early Triassic Semeitau igneous series, eastern Kazakstan. *Journal of Geophysical Research*, *107*, B72139. https://doi.org/10.1029/2001JB000521

Manzoni, M. (1970). Paleomagnetic data of middle and upper Triassic age from The Dolomites (eastern Alps, Italy). *Tectonophysics*, *10*, 411–424. https://doi.org/10.1016/0040-1951(70)90119-8

Maron, M., Muttoni, G., Rigo, M., Gianolla, P., & Kent, D. (2019). New magnetobiostratigraphic results from the Ladinian of the Dolomites and implications for the Triassic geomagnetic polarity timescale. *Palaeogeography, Palaeoclimatology, Palaeoecology*, *517*, 52–73. https://doi.org/10.1016/j.palaeo.2018.11.024

McElhinny, M. W., & Larson, R. L. (2003). Jurassic dipole low defined from land and sea data. *Eos, Transactions, American Geophysical Union*, *84*, 362–366. https://doi.org/10.1029/2003EO370003

McElhinny, M. W., & McFadden, P. L. (1997). Palaeosecular variation over the past 5 Myr based on a new generalized database. *Geophysical Journal International*, *131*(2), 240–252. https://doi.org/10.1111/j.1365-246X.1997.tb01219.x

McElhinny, M. W., & McFadden, P. L. (2000). *Paleomagnetism: Continents and oceans* (2nd ed., p. 386). Academic Press.

McFadden, P. L., & McElhinny, M. W. (1988). The combined analysis of remagnetization circles and direct observations in palaeomagnetism. *Earth and Planetary Science Letters*, *87*, 161–172. https://doi.org/10.1016/0012-821X(88)90072-6

McFadden, P. L., Merrill, R. T., & McElhinny, M. W. (1988). Dipole/quadrupole family modeling of paleosecular variation. *Journal of Geophysical Research*, *93*(B10), 11583–11588. https://doi.org/10.1029/JB093iB10p11583

McFadden, P. L., Merrill, R. T., McElhinny, M. W., & Lee, S. (1991). Reversals of the Earth's magnetic field and temporal variations of the dynamo families. *Journal of Geophysical Research*, *96*(B3), 3923–3933. https://doi.org/10.1029/90JB02275

Ogg, J. G. (2012). Geomagnetic polarity time scale. In F. M. Gradstein, J. G. Ogg, M. G. Schmitz, & G. M. Ogg (Eds.), *The geologic time scale* (pp. 85–113). Elsevier. https://doi.org/10.1016/B978-0-444-59425-9.00005-6

Ogg, J. G., Ogg, G. M., & Gradstein, M. (2016). Triassic. In J. G. Ogg, G. M. Ogg, & M. Gradstein (Eds.), *A concise geologic time scale* (pp. 133–149). Elsevier. https://doi.org/10.1016/b978-0-444-59467-9.00011-x

Olson, P., Driscoll, P., & Amit, H. (2009). Dipole collapse and reversal precursors in a numerical dynamo. *Physics of the Earth and Planetary Interiors*, *173*, 21–140. https://doi.org/10.1016/j.pepi.2008.11.010

Opdyke, N. D., & Channell, J. E. T. (1996). *Magnetic stratigraphy*. Academic Press.

Opdyke, N. D., Roberts, J., Claoué-Long, J., Irving, E., & Jones, P. J. (2000). Base of the Kiaman: Its definition and global stratigraphic sequence. *GSA Bulletin*, *112*, 1315–1341. https://doi.org/10.1130/0016-7606(2000)112<1315:BOTKID>2.0.CO;2

Pal, P. C. (1991). The correlation of long-term trends in the palaeointensity and reversal frequency variations. *Journal of Geomagnetism and Geoelectricity*, *43*, 409–428. https://doi.org/10.5636/jgg.43.409

Palencia-Ortas, A., Ruiz-Martinez, V. C., Villalaín, J. J., Osete, M. L., Vegas, R., Touil, A., et al. (2011). A new 200 Ma paleomagnetic pole for Africa, and paleo-secular variation scatter from Central Atlantic Magmatic Province (CAMP) intrusives in Morocco (Ighrem and Foum Zguid dykes). *Geophysical Journal International*, *185*, 1220–1234. https://doi.org/10.1111/j.1365-246X.2011.05017.x

Pavlov, V. E., Courtillot, V., Bazhenov, M. L., & Veselovsky, R. V. (2007). Paleomagnetism of the Siberian Traps: New data and a new over 250 Ma pole for Siberia. *Tectonophysics*, *443*, 72–92. https://doi.org/10.1016/j.tecto.2007.07.005

Pavlov, V. E., Fluteau, F., Latyshev, A. V., Fetisova, A. M., Elkins-Tanton, L. T., Black, B. A., et al. (2019). Geomagnetic secular variations at the Permian-Triassic boundary and pulsed magmatism during eruption of Siberian Traps. *Geochemistry, Geophysics, Geosystems*, *20*, 773–791. https://doi.org/10.1029/2018GC007950

Perrin, M., & Shcherbakov, V. (1997). Paleointensity of the Earth's magnetic field for the past 400 Ma: Evidence for a dipole structure during the Mesozoic low. *Journal of Geomagnetism and Geoelectricity*, *49*, 601–614. https://doi.org/10.5636/jgg.49.601

Prévot, M., El-Messaoud Derder, M., McWilliams, M., & Thompson, J. (1990). Intensity of the Earth's magnetic field: Evidence for a Mesozoic dipole low. *Earth and Planetary Science Letters*, *97*, 129–139. https://doi.org/10.1016/0012-821X(90)90104-6

Ruiz-Martinez, V. C., Torsvik, T. H., van Hinsbergen, D. J. J., & Gaina, C. (2012). Earth at 200 Ma: Global palaeogeography refined from CAMP palaeomagnetic data. *Earth and Planetary Science Letters*, *331–332*, 67–79. https://doi.org/10.1016/j.epsl.2012.03.008

Schneider, D. A., & Kent, D. V. (1990). The time-averaged paleomagnetic field. *Reviews of Geophysics*, *28*(1), 71–96. https://doi.org/10.1029/RG028i001p00071

Selkin, P. A., & Tauxe, L. (2000). Long-term variations in palaeointensity. *Philosophical Transactions of the Royal Society A: Mathematical Physical and Engineering Sciences*, *358*, 1065–1088. https://doi.org/10.1098/rsta.2000.0574

Shaar, R., & Tauxe, L. (2015). Instability of thermoremanence and the problem of estimating the ancient geomagnetic field strength from non-single-domain recorders. *Proceedings of the National Academy of Sciences of the United States of America*, *12*(36), 11187–11192. https://doi.org/10.1073/pnas.1507986112

Sharps, R., McWilliams, M., Li, Y., Cox, A., Zhang, Z., Zhai, Y., et al. (1989). Lower Permian paleomagnetism of the Tarim block, northwestern China. *Earth and Planetary Science Letters*, *92*, 275–291. https://doi.org/10.1016/0012-821X(89)90052-6

Shcherbakova, V. V., Zhidkov, G. V., Shcherbakov, V. P., Latyshev, A. V., & Fetisova, A. M. (2015). Verifying the Mesozoic dipole low hypothesis by the Siberian trap data. *Physics of the Solid Earth*, *51*, 362–382. https://doi.org/10.1134/S1069351315030155

Soffel, H. C., & Harzer, F. (1991). An upper carboniferous-lower Permian (280 Ma) palaeomagnetic pole from the western margin of the Bohemian Massif. *Geophysical journal International*, *105*, 547–551. https://doi.org/10.1111/j.1365-246X.1991.tb06733.x

Song, P., Ding, L., Lippert, P. C., Li, Z., Liyum, Z., & Xie, J. (2020). Paleomagnetism of Middle Triassic lavas from northern Qiangtang (Tibet): Constraints on the closure of the Paleo-Tethys Ocean. *Journal of Geophysical Research: Solid Earth*, *125*, e2019JB017804. https://doi.org/10.1029/2019JB017804

Sprain, C. J., Feinberg, J. M., Geissman, J. W., Strauss, B., & Brown, M. C. (2016). Paleointensity during periods of rapid reversal: A case study from the Middle Jurassic shamrock batholith, western Nevada. *GSA Bulletin*, *128*(1–2), 223–238. https://doi.org/10.1130/B31283.1

Tanaka, K., Kono, M., & Uchimura, H. (1995). Some global features of palaeointensity in geological time. *Geophysical Journal International*, *120*, 97–102. https://doi.org/10.1016/0012-821X(90)90104-6

Tarduno, J. A., & Cottrell, R. D. (2005). Dipole strength and variation of the time-averaged reversing and nonreversing geodynamo based on Thellier analyses of single plagioclase crystals. *Journal of Geophysical Research*, *110*, B11101. https://doi.org/10.1029/2005JB003970

Tarduno, J. A., Cottrell, R. D., & Smirnov, A. V. (2001). High geomagnetic intensity during the mid-Cretaceous from Thellier analyses of single plagioclase crystals. *Science*, *291*(5509), 1779–1783. https://doi.org/10.1126/science.1057519

Tauxe, L., & Kent, D. V. (2004). A simplified statistical model for the geomagnetic field and the detection of shallow bias in paleomagnetic inclinations: Was the ancient magnetic field dipolar? In J. E. T. Channel, D. V. Kent, W. Lowrie, & J. G. Meert (Eds.), *Timescales of the paleomagnetic field, geophysical monograph series* (Vol. 145, pp. 101–115). American Geophysical Union. https://doi.org/10.1002/9781118665855

Thellier, E., & Thellier, O. (1959). Sur l'intensité du champ magnétique terrestre dans le passé historique et géologique. *Annales de Geophysique*, *15*, 285.

Tomezzoli, R. N., Saint Pierre, T., & Valenzuela, C. (2009). New palaeomagnetic results from Late Paleozoic volcanic units along the Western Gondwana margin in La Pampa, Argentina. *Earth, Planets and Space*, *61*, 183–189. https://doi.org/10.1186/BF03352898

Valencio, D. A., Mendía, J. E., & Vilas, J. F. (1975). Palaeomagnetism and K-Ar ages of Triassic igneous rocks from the Ischigualasto-Ischichuca Basin and Puesto Viejo formation, Argentina. *Earth and Planetary Science Letters*, *26*, 319–330. https://doi.org/10.1016/0012-821X(75)90007-2

Vandamme, D. (1994). A new method to determine paleosecular variation. *Physics of the Earth and Planetary Interiors*, *85*(1–2), 131–142. https://doi.org/10.1016/0031-9201(94)90012-4

Van der Voo, R. (1990). The reliability of paleomagnetic data. *Tectonophysics*, *184*(1), 1–9. https://doi.org/10.1016/0040-1951(90)90116-P

Veikkolainen, T., & Pesonen, L. J. (2014). Palaeosecular variation field reversals and the stability of the geodynamo in the Precambrian. *Geophysical Journal International*, *199*, 1515–1526. https://doi.org/10.1093/gji/ggu348

Vigliotti, L., Alvarez, W., & McWilliams, M. (1990). No relative rotation detected between Corsica and Sardinia. *Earth and Planetary Science Letters*, *98*, 313–318. https://doi.org/10.1016/0012-821X(90)90033-T

Walderhaug, H. J., Eide, E. A., Scott, R. A., Inger, S., & Golionko, E. G. (2005). Palaeomagnetism and $^{40}Ar/^{39}Ar$ geochronology from the South Taimyr igneous complex, Arctic Russia: A Middle-Late Triassic magmatic pulse after Siberian flood-basalt volcanism. *Geophysical Journal International*, *163*, 501–517. https://doi.org/10.1111/j.1365-246X.2005.02741.x

Watson, G. S., & Beran, R. J. (1967). Testing a sequence of unit vectors for serial correlation. *Journal of Geophysical Research*, *72*, 5655–5659. https://doi.org/10.1029/JZ072i022p05655

Wignall, P. B. (2015). The killing seas: The great Permo-Triassic mass extinction. In *The worst of times: How life on Earth survived eighty million years of extinctions* (pp. 39–88). Princeton University Press. https://doi.org/10.2307/j.ctvc77862.8

Wynne, P. J., Irving, E., & Osadetz, k. (1983). Paleomagnetism of the Esayoo formation (Permian) of northern Ellesmere Island: Possible clue to the solution of the Nares Strait dilemma. *Tectonophysics*, *100*, 241–256. https://doi.org/10.1016/0040-1951(83)90190-7

Yuan, K., Van der Voo, R., Bazhenov, M. L., Bakhmutov, V., Alkehin, V., & Hendriks, B. W. H. (2011). Permian and Triassic palaeolatitudes of the Ukrainian shield with implications for Pangaea reconstructions. *Geophysical Journal International*, *184*, 595–610. https://doi.org/10.1111/j.1365-246X.2010.04889.x

Zhang, Y., Ogg, J. G., Franz, M., Bachmann, G. H., Szurlies, M., Röhling, H., et al. (2020). Carnian (Late Triassic) magnetostratigraphy from the Germanic Basin allowing global correlation of the Mid-Carnian Episode. *Earth and Planetary Science Letters*, *541*, 116275. https://doi.org/10.1016/j.epsl.2020.116275

Zhao, J., Huang, B., Yan, Y., & Zhang, D. (2015). Late Triassic paleomagnetic result from the Baoshan Terrane, West Yunnan of China: Implication for orientation of the East Paleotethys suture zone and timing of the Sibumasu-Indochina collision. *Journal of Asian Earth Sciences*, *111*, 350–364. https://doi.org/10.1016/j.jseaes.2015.06.033

References From the Supporting Information

Chenet, A., Fluteau, F., Courtillot, V., Gérard, M., & Subbarao, K. (2008). Determination of rapid Deccan eruptions across the Cretaceous-Tertiary boundary using paleomagnetic secular variation: Results from a 1200-m-thick section in the Mahabaleshwar escarpment. *Journal of Geophysical Research*, *113*, B04101. https://doi.org/10.1029/2006JB004635

McFadden, P. L., & Lowes, F. J. (1981). The discrimination of mean directions drawn from Fisher distributions. *Geophysical Journal International*, *67*(1), 19–33. https://doi.org/10.1111/j.1365-246x.1981.tb02729.x

Watson, G. S. (1956). A test for randomness of directions. *Geophysical Supplements to the Monthly Notices of the Royal Astronomical Society*, *7*(4), 160–161. https://doi.org/10.1111/j.1365-246X.1956.tb05561.x